

1 **A double-negative prostate cancer subtype is vulnerable to SWI/SNF-targeting degrader  
2 molecules**

3

4 Phillip Thienger<sup>1</sup>, Irene Paassen<sup>1</sup>, Xiaosai Yao<sup>2,3</sup>, Philip D. Rubin<sup>1</sup>, Marika Lehner<sup>1</sup>, Nicholas Lillis<sup>4</sup>, Andrej  
5 Benjak<sup>1</sup>, Sagar R. Shah<sup>5</sup>, Alden King-Yung Leung<sup>5</sup>, Simone de Brot<sup>6</sup>, Alina Naveed<sup>1</sup>, Bence Daniel<sup>7</sup>,  
6 Minyi Shi<sup>7</sup>, Julien Tremblay<sup>3</sup>, Joanna Triscott<sup>1</sup>, Giada Andrea Cassanmagnago<sup>8,9,10</sup>, Marco Bolis<sup>8,9,10</sup>, Lia  
7 Mela<sup>1</sup>, Himisha Beltran<sup>11</sup>, Yu Chen<sup>12,13,14</sup>, Salvatore Piscuoglio<sup>15,16</sup>, Haiyuan Yu<sup>5</sup>, Charlotte K Y Ng<sup>17,18</sup>,  
8 David A. Quigley<sup>4,19,20</sup>, Robert L. Yauch<sup>28</sup>, Mark A. Rubin<sup>1,18,21\*</sup>

9

10 <sup>1</sup>Department for Biomedical Research, University of Bern, Bern, 3008, Switzerland.

11 <sup>2</sup>Department of Molecular Oncology, Genentech, South San Francisco, CA, USA.

12 <sup>3</sup>Department of Computational Sciences, Genentech, South San Francisco, CA, USA.

13 <sup>4</sup>Department of Urology, University of California, San Francisco, CA, USA.

14 <sup>5</sup>Department of Molecular Biology and Genetics, Cornell University, Ithaca, NY, USA.

15 <sup>6</sup>COMPATH, Institute of Animal Pathology, University of Bern, Bern, Switzerland.

16 <sup>7</sup>Department of Proteomics and Genomic Technologies, Genentech, South San Francisco, CA 94080.

17 <sup>8</sup>Computational Oncology Unit, Department of Oncology, Istituto di Ricerche Farmacologiche ‘Mario  
18 Negri’ IRCCS, Via Mario Negri 2, 20156 Milano, Italy.

19 <sup>9</sup>Institute of Oncology Research, Bioinformatics Core Unit, Bellinzona, TI 6500, Switzerland.

20 <sup>10</sup>Università Della Svizzera Italiana (USI), Faculty of Biomedical Sciences, Bellinzona, Switzerland.

21 <sup>11</sup>Department of Medical Oncology, Dana-Farber Cancer Institute, Boston, Massachusetts.

22 <sup>12</sup>Human Oncology and Pathogenesis Program, Memorial Sloan Kettering Cancer Center, New York,  
23 NY, USA.

24 <sup>13</sup>Weill Cornell Graduate School of Medical Sciences, Weill Cornell Medicine, New York, NY, 10065,  
25 USA.

26 <sup>14</sup>Department of Medicine, Memorial Sloan Kettering Cancer Center, New York, NY 10065, USA.

27 <sup>15</sup>IRCCS Humanitas Research Hospital, 20089 Rozzano, Milan, Italy.  
28 <sup>16</sup>Department of Biomedicine, University Hospital Basel, University of Basel, 4001 Basel, Switzerland.  
29 <sup>17</sup>SIB Swiss Institute of Bioinformatics, Lausanne, Switzerland.  
30 <sup>18</sup>Bern Center for Precision Medicine, 3008, Bern, Switzerland.  
31 <sup>19</sup>Department of Epidemiology & Biostatistics, University of California, San Francisco, CA, USA.  
32 <sup>20</sup>Helen Diller Family Comprehensive Cancer Center, UCSF.  
33 <sup>21</sup>Inselspital, 3010, Bern, Switzerland.  
34 §Co-senior authors  
35

36 **\*Corresponding author:**

37 Mark A. Rubin, MD  
38 Murtenstrasse 28, Department for Biomedical Research, University of Bern, 3008 Bern, Switzerland  
39 mark.rubin@unibe.ch  
40

41 **Running title:** AR-negative PCa is vulnerable to SWI/SNF-targeting degraders  
42

43 **Conflict of interest statement**

44 R.L.Y., X.Y., B.D., M.S., and Ju.T. are active employees of Genentech Inc.. H.B. has served as  
45 consultant/advisory board member for Janssen, Astellas, Merck, Pfizer, Roche, Harpoon, Amgen, Bayer,  
46 Daiichi-Sankyo, Astra Zeneca, Harpoon and has received research funding (to institution) from Bristol  
47 Myers Squibb, Circle Pharma, Daiichi-Sankyo, Novartis. S.R.S. is an equity holder and member of the  
48 scientific advisory board of NeuScience, Inc., and a consultant at Third Bridge Group Limited. M.A.R has  
49 received research funding from Novartis, Roche, Ventana, Janssen, Astellas, and Eli Lilly and currently  
50 has a research collaboration agreement with Genentech Inc. M.A.R. is on the Scientific Advisory Board  
51 of Neogenomics Lab, is a Scientific Advisor and stockholder of Owkin, and co-founder of Verintas. M.A.R.

52 is a co-inventor on prostate cancer patents in the diagnostic and treatment fields, including SWI/SNF

53 (Bern/Cornell). All other authors declare no competing interests.

54 **Abstract**

55 Proteolysis targeting chimera (PROTAC) therapies degrading SWI/SNF ATPases offer a novel approach  
56 to interfere with androgen receptor (AR) signaling in AR-dependent castration-resistant prostate cancer  
57 (CRPC-AR). To explore the utility of SWI/SNF therapy beyond AR-sensitive CRPC, we investigated  
58 SWI/SNF-targeting agents in AR-negative CRPC. SWI/SNF targeting PROTAC treatment of cell lines  
59 and organoid models reduced the viability of not only CRPC-AR but also WNT-signaling dependent AR-  
60 negative CRPC (CRPC-WNT). The CRPC-WNT subgroup represents 11% of around 400,000 cases of  
61 CRPC worldwide who die yearly of CRPC. We discovered that SWI/SNF ATPase SMARCA4 depletion  
62 interfered with the master transcriptional regulator TCF7L2 (TCF4) in CRPC-WNT. Functionally, TCF7L2  
63 maintains proliferation via the MAPK signaling axis in this subtype of CRPC. These data suggest a  
64 mechanistic rationale for interventions that perturb the DNA binding of the pro-proliferative TCF7L2  
65 transcription factor (TF) and/or direct MAPK signaling inhibition in the CRPC-WNT subclass of advanced  
66 prostate cancer.

67

68 **Statement of significance**

69 Androgen receptor (AR)-negative prostate cancer (PCa) remains a clinical challenge due to the lack of  
70 targeted therapeutic options. Here, we identified a lineage-defining molecular axis in a subtype of AR-  
71 negative PCa, accounting for around 10% of castration-resistant PCa (CRPC) that can be interfered with  
72 by SWI/SNF-targeting agents.

73

74

75 **Introduction**

76 Treatment-induced shifts in cancer cell identity, known as lineage plasticity (LP), lead to the emergence  
77 of tumors that may have little to no resemblance to the treatment-naïve tumors. The increased and earlier  
78 use of potent targeted cancer therapies are responsible for the emergence of aggressive, “plastic,” and  
79 untreatable cancers. In prostate cancer (PCa), LP can manifest when androgen receptor (AR)-driven  
80 adenocarcinoma (CRPC-AR) differentiates into AR-negative CRPC, which lacks both canonical AR  
81 signaling and neuroendocrine differentiation markers (double-negative CRPC, aka DNPC) or acquires  
82 neuroendocrine features (CRPC-NE)<sup>1-3</sup>.

83

84 The epigenetic chromatin remodeling machinery complex switch/sucrose non-fermentable (SWI/SNF)  
85 orchestrates pluripotency and differentiation in embryonic stem cells<sup>4</sup>, indicating its potential to maintain  
86 self-renewal in cancer and modulate lineage plasticity. In line with this, the SWI/SNF complex is mutated  
87 in over 20% of cancers<sup>5</sup>. However, in PCa, genomic alterations in the SWI/SNF complex are rare.  
88 Regardless, we and others have observed the dysregulation in SWI/SNF ATP-dependent helicases  
89 SMARCA2 (BRM) and SMARCA4 (BRG1) expression levels in CRPC<sup>6,7</sup>. In non-small lung cancer  
90 (NSCLC), alterations in SWI/SNF ATPase expression (mainly loss of SMARCA4) have led to the  
91 discovery of a synthetic lethal relationship<sup>8-10</sup>. In CRPC-AR, degradation of the SWI/SNF catalytic  
92 ATPase subunits (SMARCA2, SMARCA4) compacts cis-regulatory elements bound by AR-associated  
93 transcription factors (TFs) leading to drastic decrease of PCa proliferation<sup>11</sup>.

94

95 Another critical pathway in cancer, especially during developmental processes, is the wingless and int-1  
96 (WNT) pathway, which is partially regulated by the SWI/SNF complex<sup>12-14</sup>. Aberrations in WNT signaling  
97 are especially prominent in colorectal cancer but also emerge in other cancer types, such as CRPC<sup>15-17</sup>.  
98 This signaling pathway can be divided into the canonical ( $\beta$ -Catenin-dependent) and non-canonical ( $\beta$ -  
99 Catenin-independent) axis<sup>18</sup>. In PCa, genetic changes in canonical WNT pathway genes are found in up  
100 to 22% of CRPC cases, while also non-canonical WNT signaling is altered in advanced PCa<sup>19,20</sup>. Further,

101 the PCa stroma is known to secrete WNT proteins that activate WNT signaling in tumor cells to promote  
102 therapy resistance<sup>21,22</sup>. Recently, Tang et al. identified a subclass of CRPC, termed CRPC-WNT, that  
103 has traits of double-negative PCa (DNPC) but is enriched for mutations in WNT signaling pathway genes,  
104 accompanied by strong pathway activation through the TF TCF7L2, among others<sup>23</sup>.

105

106 In this study, we report that targeting SMARCA2/4 downregulates this lineage-defining WNT signaling  
107 signature<sup>23</sup> in CRPC-WNT patient-derived organoids. Indeed, we found that SMARCA4 depletion led to  
108 the chromatin closure at TCF7L2 DNA binding motifs and the downregulation of TCF7L2 itself in  
109 CRPC-WNT. Further, we provide evidence that this downregulation of TCF7L2 is facilitated through  
110 closure of an active intragenic enhancer. By performing chromatin immunoprecipitation sequencing, we  
111 narrowed down the function of TCF7L2 to be involved in pro-proliferative pathways such as RAS and  
112 MEK signaling by binding to relevant gene promotor. We functionally validated that CRPC-WNT are  
113 addicted to these signaling pathways and that SMARCA2/4 degradation by A947 treatment reduces the  
114 protein levels of known MEK downstream targets.

115 This is in line with findings that described MEK signaling as a dependency in DNPC<sup>1</sup>. In summary, we  
116 found TCF7L2 to be a primary driver of CRPC-WNT, which is positively regulated by SMARCA4-  
117 dependent SWI/SNF activity to drive proliferative pathways. This study strengthens the evidence that the  
118 SWI/SNF complex plays a crucial role in advanced PCa and can be therapeutically exploited beyond AR-  
119 driven PCa adenocarcinoma.

120 **Results**

121 **SMARCA2/4 is a vulnerability in DNPC patient-derived organoids (PDO)**

122 In prior work, we discovered overexpression of SMARCA4 correlates with PCa progression, particularly  
123 neuroendocrine prostate cancer<sup>6</sup>. The testing of SMARCA2/4 targeting agents in PCa had been restricted  
124 to standard cell lines, covering only a limited representation of the commonly encountered genomic  
125 landscape and progression states seen in patients with CRPC. We posited that AR-negative CRPC may  
126 also manifest sensitivity to SWI/SNF ATPase inhibition. To address this, we used a novel PROTAC  
127 degrader, A947, that co-binds the SMARCA2/SMARCA4/PBRM1 bromodomains and the von Hippel-  
128 Lindau (VHL) ubiquitin ligase<sup>9</sup> (**Fig.1a**). This molecule has slight selectivity for SMARCA2 degradation,  
129 however at the concentrations used here it is equally potent for degradation of both ATPases within 1  
130 hour in HEK293 cells (**Fig.1b**).

131

132 A947 was tested on a panel of PCa models, including established and organoid-derived cell lines and  
133 the non-neoplastic prostate line RWPE-1 (**Fig. 1c, Supplementary Figure 1a and b**). The four CRPC  
134 subclasses described by Tang et al.<sup>23</sup>, AR-dependent (CRPC-AR) (n=6), “WNT-driven” (CRPC-WNT)  
135 (n=4), neuroendocrine prostate cancer (NEPC) (n=4), and “stem-cell-like” (CRPC-SCL) (n=7) were  
136 treated for seven days with A947 in a dose response (**Supplementary Figure 1a**). We confirmed that  
137 AR-dependent cell models are particularly sensitive to SWI/SNF degradation<sup>11</sup>. In addition, we  
138 discovered that CRPC-WNT models were fully or partially responding to A947 (area under the curve  
139 (AUC<250)) (**Fig.1c, Supplementary Figure 1a**). All PCa model systems tested were non-responsive to  
140 negative control A858 epimer (SMARCA-binding control) as expected (**Supplementary Figure 1a**). A947  
141 was able to degrade all predicted targets, SMARCA2, SMARCA4 and PBRM1 in all four CRPC-WNT  
142 models (**Supplementary Figure 1c**). Similar anti-proliferative responses as to A947 were observed with  
143 SMARCA2/4 PROTAC AU-15330 and inhibitors FHD-286 and BRM014 in all four CRPC-WNT and  
144 CRPC-AR but not in other subtypes (**Supplementary Figure 2a, b and c**). Next, we checked for  
145 SMARCA2, SMARCA4 and lineage-defining marker expression in selected organoids, as well as cell

146 lines and found the expected marker gene expression pattern, while the expression for SMARCA4 was  
147 overall higher than the expression of SMARCA2 in most models, also the ones that showed a response  
148 to A947-treatment (**Fig. 1d**).

149

150 Organoid formation was drastically reduced in CRPC-WNT organoids after 7 days of A947 treatment  
151 (**Fig. 1e and f; Supplementary Figure 2d**). Assessment of growth kinetics using live-cell imaging in  
152 CRPC-WNT 2D lines MSK-PCa16 and WCM1078 showed significant reduction in cell confluence over  
153 time to a single dose (1 $\mu$ M) of A947 compared with control epimer A858 (**Supplementary Figure 2e**).  
154 Strikingly, competition of A947 with a free VHL ligand (VL285) rescued growth inhibitory effect dose  
155 dependently (**Supplementary Figure 2f**). Notably, levels of cleaved PARP1 (Asp214) were increased in  
156 the CRPC-WNT lines, WCM1078 and MSK-PCa16 upon treatment with 1 $\mu$ M A947 indicating activation  
157 of the intrinsic pathway of cell death (**Supplementary Figure 2g**).

158

159 To estimate the necessity of SMARCA2/4 activity in the CRPC-WNT, we performed individual siRNA-  
160 mediated knockdown of these two main A947 targets in CRPC-WNT models, a CRPC-NE model and  
161 CRPC-SCL model. All CRPC-WNT models showed a strong growth inhibitory effect upon SMARCA4  
162 knockdown but only minimally responded to the knockdown of SMARCA2. CRPC-NE model WCM154  
163 and CRPC-SCL model WCM155, however, were unaffected by either siRNA knockdown  
164 (**Supplementary Figure 3a, b**). SMARCA4 inhibition has been reported to be synthetic lethal with PTEN  
165 loss in PCa<sup>24</sup>. However, only two of the four CRPC-WNT models harbor PTEN deletions, indicating that  
166 the response to SMARCA4 degradation may be independent of its PTEN status<sup>23</sup>. To rule out siRNA-  
167 mediated off-target effects, we elucidated the isolated effects of SMARCA4 depletion on cell growth using  
168 CRISPR-Cas9 sgSMARCA4 transduced organoids. We confirmed similar growth inhibition and cell-killing  
169 effect to A947 treatment upon SMARCA4 knockdown using CRISPRi in all four CRPC-WNT lines (**Fig.**  
170 **1g; Supplementary Figure 3c, d**). In conclusion, we identified an AR-negative subtype of CRPC that is  
171 dependent on the SWI/SNF ATPase SMARCA4 in vitro.

172

173 **CRPC-WNT is a clinically relevant subset of advanced CRPC**

174 To determine how frequently the CRPC-WNT phenotype identified by Tang et al.<sup>23</sup> is seen clinically, we  
175 used publicly available single-cell sequencing (scRNA-seq) data from PCa cohorts (which include normal  
176 prostate/primary PCa (n=45), CRPC/NEPC (n=29) samples in total<sup>2,25-29</sup>). We found that the four  
177 signatures described by Tang et al.<sup>23</sup> could be identified in distinct clusters, especially the CRPC-WNT  
178 signature, which appeared in two distinct subclusters of CRPC separate from all other clusters (**Fig. 1h**).  
179 All remaining signatures, CRPC-AR, CRPC-NE, and CRPC-SCL, were more broadly distributed.  
180 Surprisingly, the CRPC-SCL signature was not only highly expressed in CRPC cases but also in normal  
181 and primary PCa (**Fig. 1h**). Overall, the signatures for CRPC-AR, CRPC-WNT, CRPC-NE, and CRPC-  
182 SCL account for 38.3%, 11.7%, 22.9% and 22.4% of all CRPC cases, respectively. This underpins the  
183 clinical relevance of these signatures. These signatures could not characterize 4.7% of CRPC cases,  
184 indicating that additional rare phenotypes of CRPC may exist (**Fig. 1i**). This highlights that CRPC-WNT  
185 is a highly clinically relevant subtype of PCa for which there is no viable treatment option available. All  
186 these findings encouraged us to investigate the effect of SMARCA2/4 degradation on CRPC-WNT *in vivo*  
187

188 **Treatment with SMARCA2/4 PROTAC leads to CRPC-WNT tumor growth delay *in vivo***

189 To assess the effect of SMARCA2/4 degradation *in vivo*, we generated a mouse-adapted patient-derived  
190 xenograft subline from the WCM1078 CRPC-WNT model. Since WCM1078 did not reliably grow *in vivo*,  
191 we had to create a subline from a single WCM1078 tumor that grew only in 1 out of 5 injected mice within  
192 6 months. Tumor cells were expanded *in vitro* and injected again into mice until visible tumors formed.  
193 From these tumors, we generated cryobits. These cryobits were subcutaneously transplanted into 20  
194 mice. 16/20 of the animals developed tumors; 15 were taken into the study, and the others were excluded.  
195 A single dose of A947 treatment (40mg/kg) or vehicle was given to 8 animals or 7 animals, respectively,  
196 when tumors reached 60-80mm<sup>3</sup> (**Supplementary Figure 4a**). Before treatment, we checked the  
197 potential of A947-treatment to reduce mouse SMARCA4 paralog *in vitro*. We found that the compound is

198 active in murine lung adenoma LA4 cells (**Supplementary Figure 4b**). We observed a significant growth  
199 delay in the A947-treatment condition (n=8) compared to vehicle control (n=7), which aligns with the  
200 findings by Xiao et al.<sup>11</sup> in CRPC-AR (**Fig. 1j, Supplementary Figure 4c and d**). Moreover, the mice  
201 showed no signs of aberrant behavior or reduction in body mass throughout treatment (**Supplementary**  
202 **Figure 4e**). Histopathological assessment indicated that all examined tissues were unremarkable  
203 (**Supplementary Figure 4f**), except for histopathologic findings in the kidney. Chronic renal interstitial  
204 fibrosis and tubular atrophy were identified in two A947 treated mice where this change was mild (C14)  
205 to moderate (C11) (**Supplementary Figure 4g**). As this change is also known to occur spontaneously in  
206 laboratory mice (chronic nephropathy), it remains unknown if this lesion is related to the A947 treatment.  
207 Next, we assessed the levels of SMARCA4 in the tumors harvested at the endpoint. Quantifying the  
208 western blot signal showed a significant average reduction in SMARCA4 protein in the A947-treated  
209 tumors compared with control despite the single-time treatment (**Supplementary Figure 4h**). This  
210 indicates that A947 is highly active in vivo and can reduce CRPC-WNT tumor growth. In summary, we  
211 found that CRPC-WNT is highly responsive to a single treatment of A947 throughout a 21-day tumor  
212 growth period in vivo. These findings led us to investigate the underlying molecular mechanisms  
213 regulated by SMARCA4 in CRPC-WNT, which accounts for 11.7% of all CRPC patients.

214

### 215 **A lineage-defining WNT program is mitigated by SMARCA2/4 degradation in CRPC-WNT**

216 To untangle the transcriptomic and heterogeneous changes upon treatment with A947 in CRPC-WNT,  
217 we utilized single-cell RNA sequencing (scRNAseq) by SORT-seq<sup>30</sup>. WCM1078 and MSK-PCa16 were  
218 treated for 72h with 1µM A947 or control epimer A858. A total of 1133 WCM1078 cells and 1183 MSK-  
219 PCa16 cells in the A858-treated condition and a total of 1184 WCM1078 cells and 997 MSK-PCa16  
220 cells in the A947-treated condition passed quality control. Both PDOs demonstrated homogenous  
221 profiles with separate clusters forming based on treatment (**Fig. 2a and e**). As expected, CRPC-WNT  
222 signature score<sup>23</sup> was homogenously expressed in the A858 conditions, while this signal was  
223 significantly reduced after A947 treatment (**Fig. 2b, c, f and g**). High expression in A858 treated cells

224 was observed for an additional WNT signature score based on colorectal cancer (CRC\_WNT\_score;  
225 compiled of the genes "LGR5", "AXIN2", "ASCL2", "OLFM4", "SLC12A2", "GKN33P", "NKD1", "WIF1"  
226 although the signal was more heterogeneously expressed (**Supplementary Figure 5a and c**). This  
227 CRC-WNT score signal was significantly reduced by A947-treatment, in line with the reduced CRPC-  
228 WNT signature (**Supplementary Figure 5b and d**). However, besides these two specific WNT  
229 signatures we did not observe significant changes in other WNT-pathway signatures besides one LEF-  
230 related signature (**Supplementary Figure 5i and j**). This indicates that the genes that define those  
231 signatures might not be tied to canonical WNT signaling in CRPC-WNT. Therefore, we posit that the  
232 CRPC-WNT score is a refined lineage-specific signature comprised of known WNT TFs, such as TCF7,  
233 TCF7L2, and LEF1, that might have non-canonical functions.

234

235 Notably, other CRPC subtype signature scores (CRPC-AR, CRPC-SCL, CRPC-NE) were barely  
236 expressed in the CRPC-WNT organoids (**Supplementary Figure 5e and f**). Notably, The CRPC-SCL  
237 and CRPC-NE scores were also downregulated by A947 treatment compared with A858 treatment, but  
238 the positive clusters had low base levels compared with the CRPC-WNT positive cluster (**Supplementary**  
239 **Figure 5e and f**). This was confirmed by bulk RNA-seq data on WCM1078 after 24h and 48h with A947  
240 (**Supplementary Figure 6a**). Overall, several individual genes that define CRPC-WNT, as characterized  
241 by Tang et al.<sup>23</sup>, were downregulated upon treatment with A947 in both organoid models (**Fig. 2d and**  
242 **h**). SCENIC pathway analysis identified decreased activity of multiple TFs upon A947-treatment<sup>31</sup>. In  
243 both, WCM1078 and MSK-PCa16, activity of several TFs has been reduced; namely activity of FOX,  
244 TCF/WNT, ETV and AP-1 family members showed decreased activity (**Supplementary Figure 5g and**  
245 **h**). In agreement, bulkRNA-seq data of WCM1078 after A947 treatment showed decreased expression  
246 of a subset of the Top 25 highest-ranked transcription factors in CRPC-WNT<sup>23</sup>, among the most  
247 downregulated TFs: KLF2, TCF7L1, TCF7L2, SOX13, SOX4, RUNX3 and LEF1 (**Supplementary Figure**  
248 **6b**). Gene ontology analysis of oncogene C6 signature revealed a downregulation of MAPK signaling  
249 signatures terms (ERBB2\_UP.V1\_UP, MEK\_UP.V1\_UP) upon A947 treatment in WCM1078 cells

250 (**Supplementary Figure 5i**). Moreover, we found that in MSK-PCa16 scRNA-seq the most  
251 downregulated C6 oncogene pathways were associated with WNT (LEF1\_UP.V1\_UP) and MAPK  
252 signatures (KRAS.600\_UP.V1\_UP, KRAS.KIDNEY\_UP.V1\_UP) (**Supplementary Figure 5j**).  
253 Gene set enrichment analysis of bulk RNA-seq data of WCM1078 after 48h treatment revealed that  
254 multiple oncogene C6 signatures, associated with mitogen-activated protein kinase (MAPK)-KRAS-MEK  
255 signaling, were downregulated by A947-treatment (**Supplementary Figure 6c**). This data validates our  
256 previous finding in the scRNA-seq analysis and points to a potential MAPK-associated proliferative axis  
257 in CRPC-WNT which is disrupted by A947 treatment. This might be a downstream effect of the loss of  
258 the lineage-defining CRPC-WNT signature. To gain further insight into the epigenetic orchestration of  
259 this process, we examined chromatin accessibility in CRPC-WNT upon treatment with A947.

260

#### 261 **SMARCA2/4 degradation leads to closure of TCF/LEF chromatin binding sites in CRPC-WNT**

262 The SWI/SNF complex mediates nucleosomal DNA packaging and is actively involved in regulating gene  
263 expression of multiple programs that can be crucial for cell survival. To mechanistically exploit changes  
264 in chromatin accessibility, we profiled the changes mediated by A947 treatment using the assay for  
265 transposase-accessible chromatin followed by sequencing (ATAC-seq). Within 4 hours, we found a near-  
266 complete loss at 3,979 sites in WCM1078 (CRPC-WNT), while only 80 sites were gained compared with  
267 A858 treatment (**Fig. 2i**). The compaction of lost sites in WCM1078 organoids was comparable to what  
268 has been found in CRPC-AR cell lines upon the treatment with SMARCA2/4 PROTAC<sup>20</sup> (**Supplementary**  
269 **Figure 6d**). Overall, we see that over 50% of A947-treatment compacted sites are associated with intronic  
270 and distal intergenic regions like what has been observed in CRPC-AR<sup>20</sup> (**Fig. 2j**). Transcription factor  
271 motif analysis of A947 lost sites revealed lost motif accessibility of several CRPC-WNT driving TFs,  
272 among others: Jun-AP1, TCF, LEF, SIX, NFE, FOX, and SOX motifs (**Fig. 2k, Supplementary Figure**  
273 **7a**). The top depleted motifs upon A947 treatment are TCF7L2-related, which has been identified as the  
274 most active TF in CRPC-WNT<sup>23</sup>. Also, the motif Jun-AP1 is associated with WNT signaling factors since  
275 c-Jun is known to form a pro-proliferative complex with β-Catenin and TCF TFs, including TCF7L2<sup>32-34</sup>.

276 Moreover, SIX TFs are known to directly interact with TCF7L2 and drive PCa cell plasticity via WNT  
277 signaling<sup>35-37</sup>. The fact that we see FOX motifs downregulated aligns with the findings made in CRPC-  
278 AR, indicating also the on-target selectivity of A947<sup>20</sup>. When performing GSEA of the ATAC-seq and  
279 ATAC-seq/RNA-seq overlap results, we found that gene sets associated with MEK signaling were found  
280 to be downregulated by A947-treatment (**Supplementary Figure 7b-e**). These findings indicate that  
281 TCF/LEF signaling motifs are direct targets of the SWI/SNF complex remodeling, potentially regulating  
282 several downstream effectors associated with carcinogenesis and proliferation.

283

#### 284 **TCF7L2 is a dependency in CRPC-WNT**

285 To test if WNT signaling and TCF7L2 expression is critical for CRPC-WNT survival we performed siRNA-  
286 mediated knockdown experiments. MSK-PCa16, which has an amplification in TCF7L2, indeed showed  
287 a growth inhibitory effect upon siTCF7L2 transfection (**Fig. 3a**). This phenotype was rescued by the  
288 transfection of a transient TCF7L2 rescue construct indicating the effect of siRNA on cell confluence is  
289 not due to off-target effects (**Fig. 3a, Supplementary Figure 8a**). In line with this, spheroid formation of  
290 other CRPC-WNT models was reduced when depleting TCF7L2 and  $\beta$ -Catenin (CTNNB1) using siRNA  
291 (**Fig. 3b, Supplementary Figure 8b**). Notably, CRPC-NE and CRPC-SCL models which express  
292 TCF7L2 were unaffected by siTCF7L2 (**Supplementary Figure 8c**). To assess potential bias from the  
293 organoid growth media, which, contains R-spondin 1 (RSPO1), an activator of WNT-signaling, we  
294 measured the growth of WCM1078 and MSK-PCa16 in the absence of RSPO1 upon knockdown of  $\beta$ -  
295 Catenin and TCF7L2. The growth phenotype with and without RSPO1 showed no significant differences  
296 when transfected with siRNA against WNT TFs, and the absence of RSPO1 only marginally affected  
297 general growth rates of these PDOs (**Supplementary Figure 8d**). Indeed, a recent study has identified  
298 that RSPO1 is not the inducing factor responsible for TCF7L2 expression in WNT-driven lineage  
299 progression<sup>38</sup>. This indicates that the WNT factors TCF7L2 and  $\beta$ -Catenin are potentially activated via  
300 non-canonical mechanisms or are constitutively active in CRPC-WNT indicated by harbored mutations  
301 in several WNT signaling factors<sup>23</sup>.

302

303 We next asked if SMARCA2/4 degradation has direct impact on the expression on WNT signaling TFs.  
304 Immunohistochemical staining of CRPC-WNT organoids treated with 1 $\mu$ M of control A858 or A947 for  
305 24h revealed a strong downregulation of TCF7L2 signal (**Fig. 3c**). We found that also the SMARCA2/4  
306 PROTAC AU-15330 reduced levels of TCF7L2 over time (**Supplementary Figure 8e**). Further, protein  
307 expression of TCF7L2, TCF7 and LEF1 was reduced over time upon A947-treatment, whereas  $\beta$ -Catenin  
308 levels were unaffected (**Supplementary Figure 8f**). This led us to assess the basis of TCF7L2  
309 downregulation upon A947-treatment by looking at changes of chromatin structure.

310

### 311 **TCF7L2 expression is regulated through an active intragenic enhancer**

312 As stated previously TCF7L2 binding sites are closing upon treatment with A947 and more strikingly, we  
313 observed downregulation on the protein level by immunohistochemistry and immunoblot in MSK-PCa16  
314 and WCM1078 cells within 24h of treatment (**Fig. 3c, Supplementary Figure 8f**). Surprisingly, A947-  
315 treatment did not compact the TCF7L2 promoter loci, indicating closure of other regulatory sites lead to  
316 the downregulation of TCF7L2 levels. One of the earliest events in gene transcription is the activation of  
317 distal cis-regulatory enhancer regions and its associated transcription of eRNA. Since changes in  
318 chromatin structure are extremely rapid upon impairment of the SWI/SNF complex, it is not surprising to  
319 see the loss of accessibility of distal regulatory regions upon SWI/SNF complex inactivation<sup>39,40</sup>. Thus,  
320 we hypothesized that enhancer regions of TCF7L2 could be affected by A947-treatment.

321

322 To test our hypothesis, we explored the impact of A947-treatment on eRNA expression using the nuclear  
323 run-on followed by cap-selection assay (PRO-cap), which is the most sensitive method to identify active  
324 enhancers by measurement of endogenous eRNA transcription levels genome-wide at base-pair  
325 resolution<sup>41</sup>. Active enhancers loci can be precisely delineated by detecting active transcription start sites  
326 that are dependent on the associated core promoter sequences<sup>42</sup> (**Supplementary Figure 9a**). When  
327 treating WCM1078 organoids for 24h with A858 or A947 (1 $\mu$ M) followed by PRO-cap, we found 1069 of

328 eRNAs aka distal peaks (+/- 1kb) to be downregulated (blue) while only 2 distal peaks were upregulated  
329 (red) by A947-treatment (**Supplementary Figure 9b**). Next, we used the genomic search engine  
330 GIGGLE to identify and rank A947-treatment lost genomic loci shared between publicly available genome  
331 interval files<sup>43</sup>. These loci significantly overlapped with genomic sites bound by transcription factors  
332 associated with AP-1 (JUND, FOS, FOSL2, JUN), as well as FOXA1, ETV5, and TCF7L2 among the top  
333 20 repressed distal peaks (**Supplementary Figure 9c**).

334

335 To identify potential promoter-enhancer loops regulating TCF7L2 expression, we exploited publicly  
336 available Hi-C data of 80 CRPC biopsy samples<sup>44</sup>. From these 80 samples, one patient with the highest  
337 CRPC-WNT gene expression score was selected for further inspection. Analysis of the TCF7L2 locus  
338 showed high contact frequency of the TCF7L2 promoter (chr10:112949674-112950536) with two  
339 intragenic regions (chr10:113087027-113087928 and chr10:113093268-113094092) that displayed high  
340 PRO-cap signal in WCM1078 treated with control epimer A858 (**Supplementary Figure 9d**). PRO-cap  
341 signal in these two intragenic regions after A947 treatment was significantly reduced. Decrease in PRO-  
342 cap signal was accompanied with decreased ATAC-signal and TCF7L2 binding to these intergenic  
343 regions. Intragenic regions were previously described as potential enhancer regions for TCF7L2<sup>45,46</sup>.  
344 Based on these findings we hypothesize that TCF7L2 regulates its own expression in CRPC-WNT patient  
345 by binding of an upstream intergenic enhancer region. Moreover, upon SMARCA2/4 degradation with  
346 A947 these potential enhancer loci reduce signal in PRO-cap, TCF7L2 ChIP-seq and ATAC-seq assays,  
347 indicating closure of those sites (**Supplementary Figure 9d**). This finding indicates that TCF7L2  
348 expression is regulated by the SWI/SNF complex via maintenance of an intronic regulatory enhancer  
349 region in CRPC-WNT, similar to what has been reported for AR and FOXA1 in CRPC-AR<sup>11</sup>.

350

351 **TCF7L2 is not maintaining CRPC-WNT proliferation via traditional WNT signaling cues**

352 For this we tested if A947-treatment interfered with transactivation of the TCF/LEF reporter TOPFlash<sup>47</sup>.  
353 We generated stable organoid lines from WCM1078 that express the multimerized TCF-binding site

354 TOPFlash reporter or the negative control containing mutated TCF-binding binding sites (FOPFlash). To  
355 know if TCF7L2 or  $\beta$ -Catenin overexpression (OE) could rescue the expected downregulation of reporter  
356 signal by SMARCA2/4 PROTAC treatment, we overexpressed those two factors in the TOP/FOPFlash  
357 reporter organoids.

358

359 As expected, we found that both PROTACs, A947 and AU-15330, represses the TOPFlash reporter  
360 signal after 48h of treatment. While  $\beta$ -Catenin and TCF7L2 OE increased the reporter signal in DMSO  
361 control condition the PROTAC-treatment induced signal reduction could not be rescued in WCM1078  
362 organoid lines (**Fig. 3d, Supplementary Figure 8g**). As we saw that A947-treatment represses the  
363 expression of multiple TCF and LEF TFs within 24h it is not surprising that OE of a single factor is not  
364 enough to restore the TCF/LEF reporter signal, when multiple TFs remain depleted (**Supplementary**  
365 **Figure 8f**).

366

367 To test whether CRPC-WNT are dependent on canonical WNT signaling, we treated CRPC-WNT  
368 organoids with three WNT inhibitors that have different modes of action (LGK974 (Porcupine inhibitor)<sup>48</sup>,  
369 iCRT14 ( $\beta$ -Catenin inhibitor)<sup>49</sup>, MSAB ( $\beta$ -Catenin inhibitor leading to its degradation)<sup>50</sup>. In addition, we  
370 treated the CRPC-NE model WCM154 and CRPC-AR model LNCaP, which should be “WNT-  
371 independent”, with these drugs. To our surprise, we found that all cell models used, including the “WNT-  
372 dependent” ones, did not respond to LGK974 or iCRT14. MSAB treatment led to decreased proliferation  
373 in all cell models tested, also the “WNT-independent” ones, at approximately the same concentration,  
374 indicating potential off-target effects of this drug (**Supplementary Figure 8h**). To see if pathway activation  
375 would have a stronger effect, we tested the WNT signaling agonist CHIR99021 (GSK3 $\beta$  inhibitor) in the  
376 CRPC-WNT model. Despite a slight increase in proliferation up to 1 $\mu$ M in MSK-PCa16 and WCM1262  
377 the CRPC-WNT models were unresponsive to this agonist like we have observed with WNT agonist  
378 RSPO1 (**Supplementary Figure 8d and i**). Regardless, TCF7L2 OE enhanced growth in the WCM1078  
379 model but did not rescue the growth delay induced by A947- and AU-15330-treatment like empty vector

380 (EV) control or  $\beta$ -Catenin OE conditions (**Supplementary Figure 8j**). The fact that forced TCF7L2  
381 expression cannot rescue the phenotype is not surprising, since multiple TCF7L2 binding sites are closing  
382 upon SMARCA2/4 degradation making TCF7L2 interaction with these DNA domains impossible.

383

384 This let us hypothesize that CRPC-WNT is not driven by the canonical WNT pathway and that TCF7L2  
385 is hijacked to activate other pathways. Although these findings were unexpected, this data aligns with the  
386 fact that we do not see any canonical WNT gene sets affected by A947-treatment, despite seeing multiple  
387 WNT TFs being downregulated at the protein level over time (**Supplementary Figure 6c and 8f**). Thus,  
388 we raised the question if TCF binding sites have been reprogrammed in CRPC-WNT to drive WNT-  
389 independent pathways. Therefore, we aimed to uncover the TCF7L2 orchestrated pathways, which are  
390 affected by A947-treatment in CRPC-WNT by performing TCF7L2 ChIP-seq.

391

### 392 **SWI/SNF ATPase degradation abrogates proliferative signaling pathways tied to TCF7L2 in CRPC- 393 WNT**

394 To define the TCF7L2 cistrome in CRPC-WNT, we used chromatin immunoprecipitation followed by  
395 sequencing (ChIP-seq) analysis of WCM1078 organoids. In line with the chromatin closure at TCF7L2  
396 motif sites by ATAC-seq, we found decreased TCF7L2 binding to chromatin in WCM1078 organoids upon  
397 exposure to A947 for 4h (**Fig. 4a**). A947 treatment led to the loss of 4,393 sites compared with the A858  
398 control. Of the 4,393 lost TCF7L2 sites, 1,903 showed overlap with closing chromatin regions detected  
399 by ATAC-seq, representing a significant proportion of downregulated ChIP-seq (43%) and downregulated  
400 ATAC-seq peaks (48%). As expected, the top depleted motifs upon A947-treatment in the TCF7L2 ChIP-  
401 seq are associated with LEF and TCF7L2 (**Supplementary Figure 10a**). This indicates that SMARCA2/4  
402 degradation indeed interferes with TCF7L2 chromatin binding.

403

404 Gene-set enrichment analysis (GSEA) of the 1903 genes overlapping between ATAC-seq and TCF7L2  
405 ChIP-seq revealed enrichment of depleted peaks in regions associated with proliferative genes, including

406 previously identified MAPK-associated pathways (RAF\_UP.V1\_DN, EGFR\_UP.V1\_UP,  
407 RAF\_UP.V1\_UP, MEK\_UP.V1\_UP) (**Supplementary Figure 10b**). GSEA of the intersect of RNA-seq,  
408 ATAC-seq, and ChIP-seq (350 genes) resulted in the top downregulated pathway being MEK signaling  
409 (**Fig. 4b**). To understand if CRPC-WNT is dependent on the MAPK-MEK signaling axis, we checked how  
410 A947-treatment transcriptionally affects genes that define the so-called MAPK pathway activity score  
411 (MPAS)<sup>51</sup>. MPAS contains a set of MAPK downstream targets that selectively predict sensitivity to MEK  
412 inhibitors (MEKi) in multiple cancer types. Interestingly, DNPC has previously been described as sensitive  
413 to MEKi and FGFR1 inhibition<sup>1</sup>. Moreover, inhibition of MEK or FGFR1 led to downregulation of the gene  
414 transcripts making up the MPAS signature (e.g., ETV4, ETV5, DUSP4, SPRY2) in models of DNPC<sup>1</sup>.  
415 Indeed, when checking the expression of MPAS genes from RNA-seq data upon A947-treatment, we  
416 found that almost all these transcripts were downregulated in the CRPC-WNT model WCM1078  
417 (**Supplementary Figure 11a**). This was confirmed on the protein level in WCM1078 and MSK-PCa16  
418 CRPC-WNT lines when treating the cells with A947 or AU-15330 (**Fig. 4c, Supplementary Figure 11b**).  
419 Since the downregulation of MPAS proteins happened only after 24h of A947 treatment, we postulate  
420 this effect is downstream of TCF7L2 downregulation (which already happens within 1h) (**Fig. 3e**). ChIP-  
421 seq of TCF7L2 confirmed binding of promoter regions of MPAS genes (**Supplementary Figure 12a-d**).  
422 Further, we found that TCF7L2 also binds the promotor of SMARCA4 but not SMARCA2 or PBRM1. This  
423 binding is reduced upon the treatment with A947 (**Supplementary Figure 12e-g**). We also found reduced  
424 binding at the SIX2 promotor in the A947-treatment condition (**Supplementary Figure 12h**). SIX2 is  
425 known to be a TCF7L2 interactor and has implications in PCa lineage identity<sup>23,52</sup>. Lastly, we tested if  
426 the MPAS is indeed predictive for sensitivity to MEK inhibition in CRPC-WNT. For this, we used MEK  
427 inhibitor Cobimetinib alone or in combination with A947 or SMARCA2/4 inhibitor FHD-286 in CRPC-WNT,  
428 CRPC-NE, and CRPC-SCL lines. We found that Cobimetinib alone and in combination with SMARCA2/4  
429 interfering agents was most active in CRPC-WNT (**Fig. 4d**). These results were recapitulated with  
430 another MEK inhibitor, Trametinib (**Supplementary Figure 11c**).  
431

432 Thus, we conclude that the SWI/SNF complex directly shapes the cistrome for WNT signaling  
433 transcription factor TCF7L2 in AR-negative CRPC-WNT to drive pro-proliferative pathways that are  
434 predictive of MEK inhibitor sensitivity.

435

436

### 437 **Discussion**

438 The standard approach to treating advanced prostate cancer has been to modulate the AR axis either  
439 through direct or indirect means<sup>53</sup>. Drugs such as enzalutamide or abiraterone are potent androgen-  
440 receptor signaling inhibitors (ARSi) used clinically, and other agents, including AR-degraders, are in  
441 clinical development. Resistance to ARSi therapy manifests in manifold ways (e.g., *AR* gene mutation,  
442 amplification, enhancer amplification), as well as a subset acquiring epigenetic rewiring towards AR-  
443 negative phenotypes<sup>7</sup>.

444 As mentioned, AR-negative PCa had previously been classified as CRPC-NE or DNPC. CRPC-NE is  
445 characterized by a small-cell morphology, stemness, and the expression of neuronal and NE marker  
446 genes; however, while DPNC is also AR-negative, it shows no evidence of neuroendocrine differentiation  
447 based on morphology or expression of classical NE markers<sup>1,54</sup>. From this classification emerged two  
448 novel subtypes that branch into the DNPC category: CRPC-WNT and CRPC-SCL<sup>23</sup>. Tang et al.  
449 suggested that CRPC-WNT is TCF/LEF TF driven, while CRPC-SCL is YAP/TAZ TF dependent.  
450 Unfortunately, targeting these specific pathways directly remains a clinical challenge<sup>55,56</sup>. An alternative  
451 approach is to interrupt master transcriptional lineage programs by targeting TF cofactors and associated  
452 epigenetic regulators. Among these epigenetic regulators is the chromatin remodeler SWI/SNF complex,  
453 which we have previously found to be dysregulated in PCa throughout disease progression and thus  
454 represents a viable therapeutic target in early but also late-stage disease<sup>6</sup>. The SWI/SNF complex has  
455 been linked to being a predominant orchestrator of lineage-defining transcriptional programs, especially  
456 in master TF-addicted cancers<sup>57</sup>.

457 A recent study in AR-dependent PCa found that PROTAC degraders that target the SWI/SNF complex  
458 disrupt the enhancer and promoter looping interaction that wire supra-physiological expression of  
459 lineage-driving oncogenes, including the AR, FOXA1, and MYC<sup>11</sup>. However, the number of AR-negative  
460 models tested in this study were limited; therefore, we examined the effect of SWI/SNF ATPase PROTAC  
461 degraders in a PCa-focused screen. We utilized both AR-dependent and a broad spectrum of AR-  
462 negative PCa model systems, including CRPC-NE, CRPC-WNT, and CRPC-SCL. Here, we report that  
463 VHL-dependent degraders for SWI/SNF ATPase components decrease proliferation and spheroid  
464 formation in organoids of the CRPC-WNT phenotype for which no standard-of-care treatment exists.  
465 Clinically, CRPC-WNT tumors account for around 10-11% of all CRPC cases (Fig. 1i)<sup>9,11,23</sup>. We found  
466 that the SWI/SNF ATPase SMARCA4, but not SMARCA2, is a dependency in the CRPC-WNT phenotype  
467 in vitro and in vivo.

468  
469 Mechanistically, we identified that the activity of intestinal stem cell factor TCF7L2, the most active TF in  
470 CRPC-WNT<sup>23</sup>, to be attenuated upon degradation of SMARCA2/4. To our surprise CRPC-WNT models  
471 did not respond to classical ways of WNT inhibition. This indicates that TCF7L2 is involved in maintaining  
472 a niche of DNPC but potentially via non-canonical, “nontraditional” roles of TCF/LEF signaling. In line  
473 with this, we discovered that A947-treatment reduces TCF7L2 binding to MAPK-associated gene  
474 promotor. This indicates that TCF7L2 potentially gets hijacked from its traditional role in canonical WNT  
475 signaling to assist in driving MAPK transcriptional circuits. In line with these findings canonical WNT  
476 signaling has not been nominated as driver of DNPC, emphasizing that TCF7L2 has different roles in the  
477 DNPC subtype termed CRPC-WNT<sup>1</sup>. Further, a link between reported Ras pathway activation and  
478 TCF7L2 has been reported<sup>58</sup>. This is underpinned by the finding that MAPK signaling is a dependency in  
479 DNPC and that clinical trials with MEKi Trametinib in CRPC have entered Phase II (**NCT02881242**)<sup>1,59</sup>.  
480 However, these trials were not biomarker-based and were conducted in patients who progressed after  
481 AR-targeted therapy. Thus, based on our data, it may be beneficial to clinically assess the utility of the

482 CRPC-WNT score as a biomarker in CRPC to predict response to SMARCA4 or MAPK targeting  
483 therapies.

484

485 In summary, we nominated the SWI/SNF chromatin remodeling complex, primarily SMARCA4, as a  
486 vulnerability in DNPC classified as CRPC-WNT. Impaired maintenance of chromatin accessibility by  
487 SMARCA4-containing SWI/SNF complexes potentially blocks the binding of TCF7L2 on the chromatin  
488 leading to reduced pro-proliferative pathway activity (**Fig. 4e**). Paralleling other studies in CRPC and  
489 small-cell lung cancer (SCLC), our data suggests that SWI/SNF-targeting agents have general efficacy  
490 in cancers that are strongly driven by nuanced master transcriptional regulators<sup>11,60</sup>. Further, we posit  
491 that MEK inhibition could be another viable approach to target CRPC-WNT and potentially other DNPC  
492 subtypes and anticipate a mechanistic connection in future work, as indicated in previous studies<sup>1,2</sup>. We  
493 recognize, more in-depth mechanistic studies need to be conducted in this PCa phenotype to fully  
494 understand the underlying complex role of TCF7L2.

495

496 **Methods**

497 **Cell lines and compounds**

498 PCa cell lines (LNCaP, 22Rv1, VCaP, PC3, DU145, NCI-H660, C4-2), other cell lines (HEK293T, DLD1)  
499 and benign prostate line (RWPE-1) were purchased from ATCC and maintained according to ATCC  
500 protocols. Patient-derived CRPC organoids (WCM and MSK) were established and maintained as  
501 organoids in Matrigel drops according to the previously described protocol<sup>61</sup>. LNCaP-AR cells were a  
502 kind gift from Dr. Sawyers and Dr. Mu (Memorial Sloan Kettering Cancer Center) and were cultured as  
503 previously described<sup>62</sup>. All used cell lines and their phenotype are listed in Supplementary Table 1. Cell  
504 cultures were regularly tested for *Mycoplasma* contamination and confirmed to be negative. Genentech  
505 Inc. synthesized A947, its epimer (A858), FHD-286 and AU-15330. Cobimetinib, Trametinib, VL285,  
506 MBAS and CHIR99021 were purchased from SelleckChem. BRM014, LGK974 and iCRT14 were  
507 purchased from MedChemExpress. All drugs used in this study are listed in Supplementary Table 2.

508

509 **Western blot**

510 Whole-cell lysates were prepared in 1x Cell lysis buffer (CST, 9803) supplemented with protease and  
511 phosphatase inhibitor cocktail (Thermo Fisher, 78440), and total protein was measured by Pierce BCA  
512 Protein Assay Kit (ThermoFisher Scientific, 23225). An equal amount of protein was loaded in SureBlot  
513 10% or 4 to 15%, Bis-Tris Protein Gel (GenScript), and blotted. Subsequently, the nitrocellulose  
514 membrane was incubated with primary antibodies overnight in a cold room, shaking. Following incubation  
515 with HRP-conjugated secondary antibodies, membranes were imaged on a Vilber Fusion FX imager.  
516 Antibodies are listed in Supplementary Table 3.

517

518 **Xenograft experiment and pathological assessment**

519

520 *Mice*

521 Male NSG (NOD.Cg-Prkdcscid Il2rgtm1Wjl/Sz) mice at the age of 3-5 weeks were purchased from  
522 Charles River laboratories.  
523 Mice were allowed to acclimate for 2 weeks before being used for experiments.  
524 All animal studies were approved by the Cantonal Veterinary Ethical Committee, Switzerland (license  
525 BE35/2024). Animals were housed in ventilated cages with unrestricted access to presterilized food  
526 and fresh water. A maximum of five animals were maintained per cage on Aspen bedding. The ambient  
527 temperature was  $20^{\circ}\text{C} \pm 2^{\circ}\text{C}$ , kept at a constant humidity of  $50\% \pm 10\%$ , and on a 12- hour automatic  
528 light-dark cycle.

529 *A947 administration*

530 Animal was restrained in injection cone for procedure and tail was warmed in  $37^{\circ}\text{C}$  autoclaved water  
531 following disinfection of the tail before injection. Vein was visualized by slightly rotation of the tail.  
532 Injection was done with 30-gauge needle into one of the lateral veins of the mouse tail.  
533 Injection (5ul/g) was processed slowly without aspiration.  
534 After withdrawal of the needle, injection site was carefully compressed with sterile tissue to stop  
535 eventual bleeding. Animal was checked and returned to its home cage afterwards.  
536 A947 (40mg/kg) compound was prepared sterile in 10% Hydroxypropyl- $\beta$ -cyclodextrin and 50mM  
537 sodium acetate in water (pH 4.0) freshly on the day of injection.

538

539 *In vivo experimental design*

540 Tumor fragments (from organoid line WCM1078) were transplanted into NSG mice.  
541 Tumor reached measurable size ( $60-80\text{mm}^3$ ) after 16 days and mice were treated one-time with A947  
542 compound or vehicle intravenously into the lateral tail vein on day 19.  
543 Mice were monitored 3x times per week as well as tumor size was evaluated by digital caliper.

544 The volume of the tumors was calculated using the formula  $4/3\pi*((\sqrt{L*W})/2)^3$ , where L is the minor  
545 tumor axis and W is the major tumor axis. The maximal subcutaneous tumor size/burden allowed  
546 ( $1000\text{ mm}^3$ ) was not exceeded in this study. Tumors and organs were harvested freshly 21 days after  
547 treatment. Fresh tissue was snap-frozen and an additional tissue sample was fixed in Formalin (10%)  
548 for paraffin embedding. Paraffin embedded tissue was cut and stained with Hematoxylin and eosin  
549 stain for blinded histopathologic assessment by a board-certified veterinary pathologist (S.d.B.).  
550 Throughout the study one animal had to be excluded due to a bacterial infection.

551

## 552 **Immunohistochemistry**

553 Matrigel-extracted organoids were air-dried and subsequently baked at  $62\text{ }^\circ\text{C}$  for 25min.  
554 Immunohistochemistry (IHC) was performed on sections of formalin-fixed paraffin-embedded organoids  
555 (FFPE) using a Bond automated immunostainer and the Bond Polymer Refine detection system (Leica  
556 Microsystems, IL, USA) by the Translational Research Unit (TRU) platform, Bern. The TCF7L2 antibody  
557 (Cell Signaling Technologies, cat# 2569) was used for staining. The intensity of nuclear immunostaining  
558 was evaluated on whole slide tissue sections by a pathologist (S.d.B.) blinded to additional pathological  
559 and clinical data.

560

## 561 **Cell viability assay**

562 Cells and organoids were plated in 2D onto coated 96-well plates in their respective culture medium and  
563 incubated at  $37\text{ }^\circ\text{C}$  in an atmosphere of 5% CO<sub>2</sub>. After overnight incubation, a serial dilution of  
564 compounds was prepared and added to the plate. The cells were further incubated for 7 days, and the  
565 CellTiter-Glo assay (Promega) was then performed according to the manufacturer's instructions to  
566 determine cell proliferation. The luminescence signal from each well was acquired using the Varioskan  
567 LUX Plate Reader (Thermo Fisher), and the data were analyzed using GraphPad Prism software  
568 (GraphPad Software).

569

570 **Classification of CRPC subtypes from publicly available tumor data**

571 Raw data in FASTQ format were obtained from the respective sources (Table 1.) and aligned against the  
572 latest human (GRCh38) genome assembly release. Per-sample alignment and generation of feature-  
573 barcode matrices were carried out using the STAR-solo algorithm (STAR version 2.7.10b), tailored to the  
574 specific sequencing chemistry and the length of cell<sup>63</sup> barcodes and unique molecular identifiers (UMIs)  
575 on a case-by-case basis. We then imported the output feature-barcode matrices in an R environment (R  
576 version 4.0.2) and created individual Seurat objects for each sample (Seurat package version 4.0.3)<sup>64-66</sup>.  
577 A first round of quality filtering was performed through scuttle package (version 1.8.1)<sup>67</sup> by discarding  
578 outlier and low-quality cells after inspection of commonly used cell-level metrics (i.e., library size, UMI  
579 counts per cell, features detected per cell, mitochondrial and ribosomal counts ratio). Further doublet  
580 estimation and removal through the DoubletFinder prediction tool (version 2.0.3)<sup>68</sup> allowed us to drop  
581 unnecessary confounding technical artifacts. Thus, we merged our polished samples into a unique Seurat  
582 object. Seurat global-scaling normalization and log-transformation method were applied to the complete  
583 expression matrix, followed by the selection of highly variable features and linear transformation to  
584 prepare the data for dimensional reduction. The latter scaling step also allowed us to regress out  
585 unwanted sources of heterogeneity, such as mitochondrial contamination and uneven library sizes. Thus,  
586 we determined the optimal number of principal components (PCs) as the lower dimension exhibiting a  
587 cumulative percentage of variation greater than 90% to be 82. Uniform manifold approximation and  
588 projection (UMAP) based on the previously selected PCs was used to reduce dimensionality and  
589 visualize the organization and clustering of cells. Specifically, we applied a graph-based unsupervised  
590 approach coupled with the Louvain clustering algorithm implemented in Seurat to generate cell clusters.  
591 We evaluated several levels of granularity through clustree (package version 0.5.0)<sup>69</sup> resolution stability  
592 analysis to accurately depict the intrinsic cellular heterogeneity. A clustering resolution of 1 was chosen,  
593 and markers identification was conducted by taking advantage of a hurdle model designed explicitly for  
594 scRNA-seq data and implemented in the MAST statistical framework<sup>70</sup>, followed by a Bonferroni p-value  
595 adjustment to correct for multiple testing. Only genes expressed by at least 70% of cells in the cluster,

596 displaying a significant adjusted p-value (`pval_adj < 0.05`) and a solid logarithmic fold change (`log2FC >`  
597 1) were deemed as appropriate markers. After marker-based annotation of major cellular populations,  
598 we separated our collection, keeping only epithelial and malignant clusters, encompassing  
599 healthy/normal specimens of primary and castration-resistant tumors. The subsetted cells were again  
600 subjected to normalization and rescaling, and the relative UMAP was generated using 82 PCs, as before.  
601 Graph-based clustering was performed, and a granularity resolution of 0.3 was chosen, resulting in 34  
602 clusters. In-depth annotation was assigned through marker identification. Therefore, we focused on  
603 determining which clusters could be associated with the activation of specific biological pathways by  
604 assessing the enrichment score (through `AddModuleScore` function) of some recently identified  
605 signatures<sup>23</sup> in the CRPC setting, such as AR, neuroendocrine (NE), stem-cell-like (SCL) and WNT-  
606 signaling. The Seurat object was then converted into an `anndata` object, and the Scanpy (version 1.9.5)<sup>71</sup>  
607 toolkit was used for visualization.

608

#### 609 **Transfection and siRNA-mediated Knockdown**

610 ON-TARGET plus siRNA SMARTpool siRNAs against SMARCA4 (*L-010431-00-0005*), SMARCA2 (*L-*  
611 *017253-00-0005*), *CTNNB1* (*L-003482-00-0005*), *TCF7L2* (*L-003816-00-0005*) *and control* (*D-001810-*  
612 *10-05*) were purchased from Dharmacon. Reverse Transfection was performed in 6-well plates using the  
613 Lipofectamine 3000 reagent (Thermo Fisher Scientific) to the proportions of 2  $\mu$ L of 20  $\mu$ M siRNA per  
614 well. After overnight incubation, 5,000 cells were seeded triplicates in a clear 96-well plate, and  
615 confluence was monitored using IncuCyte S3 for up to 7 days. The remaining cells were harvested for  
616 protein extraction 96 h after transfection.

617

#### 618 **siRNA rescue experiment**

619 Rescue sequences (Supplementary Table 4) for the siTools against TCF7L2 (pool of 30 siRNAs) were  
620 designed and purchased from siTools Biotech. The rescue plasmid for TCF7L2 was synthesized and  
621 purchased from Atum Bio. Reverse Transfection of rescue plasmid was performed in 6-well plates using

622 the Lipofectamine 3000 reagent (Thermo Fisher Scientific) to the proportions of 5  $\mu$ L of 2  $\mu$ g plasmid per  
623 well. After overnight incubation, cells were transfected with siTools TCF7L2 siRNA pool using the  
624 Lipofectamine RNAiMAX reagent (Thermo Fisher Scientific) to the proportions of 2  $\mu$ L of 20nM siRNA  
625 per well. After overnight incubation, 5,000 cells were seeded triplicates in a clear 96-well plate, and  
626 confluence was monitored using IncuCyte S3 for up to 7 days. The remaining cells were harvested for  
627 protein extraction 96 h after Transfection. Sequences of siRNA and rescue sequence are shown  
628 Supplementary Table 4.

629

630 **Lentiviral transduction of sgRNA into organoids**

631 Organoids were transduced with CRISPRmod CRISPRi All-in-one Lentiviral hEF1a sgRNA against  
632 SMARCA4 particles (sgRNA1: VSGH12442-253241676, sgRNA2: VSGH12442-253150712, sgRNA3:  
633 VSGH12442-253336788) or control (VSGC12547). Briefly, 5 $\mu$ l of concentrated virus was added to  
634 500000 cells in suspension with TransDux MAX Lentivirus Transduction Reagent (SBI, LV860A-1) and  
635 spinfected at 600 x g, 1h, 32°C. Subsequently, they were incubated 4h at 37°C before careful seeding  
636 into Matrigel drops (50000 cells per drop) and topped up with appropriate media. Two days after  
637 transduction, virus-integrated cells were selected with puromycin. Sequences for sgRNAs are listed in  
638 Supplementary Table 6.

639

640 **Incucyte growth assays**

641 *2D monolayer formation*

642 A total of 5,000 cells per well were seeded in clear 96-well plates. After overnight incubation, compounds  
643 were added at indicated concentrations. Plates were read in an IncuCyte S3. Every 6h, phase object  
644 confluence (percentage area) for cell growth was measured. Growth curves were visualized using  
645 GraphPad.

646

647 *3D organoid formation*

648 Twenty thousand cells per well were seeded in Matrigel drops using a clear 48-well plate. After 48h  
649 incubation, compounds were added at indicated concentrations. Plates were read in an IncuCyte SX5.  
650 Every 6h, organoid object count ( $\mu\text{m}^2/\text{image}$ ) for organoid formation was measured. Growth curves were  
651 visualized using GraphPad.

652

653 **TOPFlash reporter assay**

654 WCM1078 cells were transduced with FOPFlash reporter (LTV-0011-4N, LipExoGen) or TOPFlash  
655 reporter (LTV-0011-4S, LipExoGen). After selection with Blasticidin cells were transduced with internal  
656 control Renilla Luciferase (Rluc) Lentivirus (BPS Biosciences, 79565-G). After selection with G418, cell were  
657 transduced with lentivirus to overexpress the empty vector (GeneCopoeia, NEG-LV105), CTNNB1  
658 (GeneCopoeia, CLP-I4822-LV105-200) or TCF7L2 (GeneCopoeia, CLP-I6388-LV105- 200-GS). After  
659 selection with Puromycin, the cells were seeded in triplicates (5000 cells/well) in a 96-well plate. 24h later  
660 cells were treated with either DMSO, 1 $\mu\text{M}$  A947 or 1 $\mu\text{M}$  AU-15330. 48h later, TOPFlash Firefly signal  
661 and Renilla internal control signal was detected using the Dual-Glo Luciferase Assay system (Promega,  
662 E2920). Luminescence was read using the Varioskan LUX plate reader (Thermo Fisher) and relative  
663 luminescence was calculated dividing Firefly with the Renilla luciferease signal. Graphs were were  
664 visualized using GraphPad.

665

666 **Single-cell RNA-sequencing by SORT-seq library generation and analysis**

667 SORT-seq was performed using Single Cell Discoveries (SCD) service. Organoids were treated for 72h  
668 with a control epimer (A858) or active compound (A947) at 1  $\mu\text{M}$ , and 1x10e6 cells were harvested in  
669 PBS. Harvested cells were stained with 100ng/ml DAPI to stain dead cells. Using a cell sorter (conducted  
670 by Flow Cytometry Core, DBMR, Bern) and the recommended settings (Single Cell Discoveries B.V.),  
671 DAPI-negative cells were sorted as single cells in 376 wells of four 384-well plates containing immersion  
672 oil per condition. Resulting in a theoretical cell number of 1504 cells per condition. All post-harvesting

673 steps were performed at 4°C. Plates were snap-frozen on dry ice for 15 minutes and sent out for  
674 sequencing at Single Cell Discoveries B.V.

675

676 Data were analyzed using the Seurat package v.4.3.0<sup>72</sup>. Cell QC filtering was done using the following  
677 thresholds: nCount > 4000, nFeature > 1000, percent.mito < 25, log10GenesPerUMI > 0.85. Differential  
678 gene expression analysis between clusters was done with Seurat::FindAllMarkers. Module scores were  
679 generated with Seurat::AddModuleScore. Gene set enrichment analysis was done with the package  
680 fgsea v.1.24.0<sup>73</sup> and the human gene sets from the Molecular Signatures Database (<https://www.gsea-msigdb.org>). Gene regulatory networks analysis was done with pySCENIC v.0.12.1<sup>74</sup>. Overall analysis  
681 was done in R v.4.2.2.

683

#### 684 **RNA-seq library generation and processing**

685 For bulk RNA-seq, organoids were treated with A858 or A947 (1µM) for 24h and 48h (3 biological  
686 replicates per condition). RNA was extracted using the RNeasy Kit (Qiagen); library generation and  
687 subsequent sequencing was performed by the clinical genomics lab (CGL) at the University of Bern.  
688 Sequencing reads were aligned against the human genome hg38 with STAR v.2.7.3a<sup>75</sup>. Gene counts  
689 were generated with RSEM v.1.3.2<sup>76</sup>, whose index was generated using the GENCODE v33 primary  
690 assembly annotation. Differential gene expression analysis was done with DESeq2 v.1.34.0<sup>77</sup>. Gene set  
691 enrichment analysis was done with the package fgsea v.1.20.0<sup>73</sup> and the human gene sets from the  
692 Molecular Signatures Database (<https://www.gsea-msigdb.org>). Analysis was done in R v.4.1.2.

693

#### 694 **TCF7L2 ChIP-seq library generation and processing**

695 For the ChIP-Seq assay, chromatin was prepared from 2 biological replicates of WCM1078 treated with  
696 A858 or A947 (1µM) for 4h, and ChIP-Seq assays were then performed using an antibody against  
697 TCF7L2 (Cell Signalling, cat# 2569). ChIP-seq sequence data was processed using an ENCODE-  
698 DC/chip-seq-pipeline2 -based workflow (<https://github.com/ENCODE-DCC/chip-seq-pipeline2>). Briefly,

699 fastq files were aligned on the hg38 human genome reference using Bowtie2 (v2.2.6) followed by  
700 alignment sorting (samtools v1.7) of resulting bam files with filtering out of unmapped reads and keeping  
701 reads with mapping quality higher than 30. Duplicates were removed with Picard's  
702 MarkDuplicates (v1.126) function, followed by indexation of resulting bam files with samtools. For each  
703 bam file, genome coverage was computed with bedtools (v2.26.0), followed by the generation of  
704 bigwig (wigToBigWig v377) files. Peaks were called with macs2 (v2.2.4) for each treatment sample using  
705 a pooled input alignment (.bam file) as control. Downstream analyses were performed with DiffBind  
706 v3.11.1 with default parameters, except for `summits=250` in `dba.count()`. `dba.contrast()` and  
707 `dba.analyzed()` were used to compute significant differential peaks with DESeq2.

708

#### 709 **ATAC-seq library generation and processing**

710 ATAC-seq was performed from 50'000 cryo-preserved cells per condition (1 $\mu$ M A858 and 1 $\mu$ M A947, n  
711 = 3 biological replicates) treated for 4h and analyzed as described in previous study<sup>78</sup>. Briefly, 50,000  
712 cryo-preserved cells per condition were lysed for 5 minutes on ice and fragmented for 30 minutes at 37°C,  
713 followed by DNA isolation. DNA was barcoded and amplified before sequencing.

714

#### 715 **PRO-cap library generation and processing**

716 For PRO-cap, approximately 30 million cells were processed per sample as previously described<sup>79,80</sup>.  
717 Library preparations for two biological replicates were performed separately. Cells were  
718 permeabilized, and run-on reactions were performed. After RNA isolation, two adaptor ligations and  
719 reverse transcription were performed with custom adaptors. Between adaptor ligations, cap state  
720 selection reactions were carried out using a series of enzymatic steps. RNA washes,  
721 phenol:chloroform extractions and ethanol precipitations were conducted between reactions. All steps  
722 were performed under RNase-free conditions. Libraries were sequenced on Illumina's NovaSeq lane  
723 following PCR amplification and library clean-up. Raw sequencing data was processed as previously  
724 described<sup>81</sup>. Briefly, sequencing data was trimmed with fastp version 0.22.0 and then aligned to the

725 human genome (hg38) concatenated with EBV and human rDNA sequences (GenBank U13369.1) using  
726 STAR V2.7.10b. Raw alignments were filtered with samtools version 1.18 and deduplicated using  
727 umi\_tools version 1.1.2. Alignments were converted to bigwig files using bedtools version 2.30.0 and  
728 kentUtils bedGraphToBigWig V2.8. Peaks were called using PINTS version 1.1.6<sup>41</sup>. Divergent peaks not  
729 overlapping with TSS +/-500 bp (GENCODE V37) were regarded as candidate enhancer RNAs. GIGGLE  
730 is a genomics search engine that identifies and ranks the significance of shared genomic loci between  
731 query features and thousands of genome interval files (in our case a database of ChIP-seq experiments).  
732 A higher GIGGLE score means a stronger overlap between query features and features from the  
733 database (in our case a ChIP-seq experiment from the Cistrome database). Downstream analysis was  
734 done in R v.4.2.2. Heatmaps were generated with deepTools v.3.5.0.

735  
736 Peaks were annotated with HOMER v.4.11 (<http://homer.ucsd.edu/>). Distal peaks were defined as  
737 those peaks in known introns and intergenic regions, and over 2 kb upstream or downstream from  
738 known transcription start sites. GIGGLE scores were generated at <http://dbtoolkit.cistrome.org>. Analysis  
739 was done in R v.4.2.2. Heatmaps were generated with deepTools v.3.5.0.

740  
741 **TCF7L2 enhancer analysis**  
742 Hi-C and RNA-seq data for 80 mCRPC biopsies had previously been generated by the Feng lab. Using  
743 the gene markers established by Tang et al., we classified these samples into four subtypes: Stem Cell-  
744 like (SCL), Neuroendocrine (NE), Androgen Receptor-dependent (AR), and Wnt-signaling dependent  
745 (WNT), based on the mean log expression of the designated marker genes. Among the 80 samples,  
746 only three—DTB-135-PRO, DTB-218-BL, and DTB-130-BL—fell into the WNT category. Of these, only  
747 DTB-135-PRO had a Hi-C cis interaction depth exceeding  $1 \times 10^8$ , making it the only viable sample for  
748 studying enhancer-promoter interactions in WNT signaling. Using the high-quality DTB-135-PRO  
749 dataset, we then applied ICE normalization, as previously described by G. Zhao et al., to our Hi-C  
750 matrices at a 10 kb resolution. We examined a  $\pm 500$  kb region surrounding the *TCF7L2* locus and

751 assessed Hi-C contact frequencies within A858 PRO-cap regions scoring above 10. Notably, the  
752 *TCF7L2* promoter exhibited the highest contact frequency (10.1) with the suspected enhancer between  
753 chr10:113090000-113100000 region in the DTB-135-PRO sample.

754

755

756 **Data availability**

757 RNA-Seq, ChIP-Seq, ATAC-Seq, and PRO-cap data were deposited at the Zenodo database  
758 ([10.5281/zenodo.15267271](https://doi.org/10.5281/zenodo.15267271)).

759

760 **Acknowledgments**

761 We thank the Translational Research Unit (TRU) and the Clinical Genomics Lab (CGL) of the University  
762 of Bern for their services. Further, we thank Charles Sawyers (Memorial Sloan Kettering) for the  
763 LNCaP-AR cell line. We thank Joanna Cyrtà (Institut Curie, Paris) for her commentary and suggestions.  
764 We are grateful for the project funding by the Bern Centre for Precision Medicine (BCPM) and the Peter  
765 and Traudl Engelhorn Foundation. Scientific computing was partly performed on sciCORE - Scientific  
766 Computing Center at the University of Basel. Further, we acknowledge Mariana Ricca for her help  
767 editing and preparing this manuscript. We thank Michael Berlin at Arvinas Inc. for assistance with  
768 chemical synthesis. D.A.Q. acknowledges funding from the Benioff Initiative for Prostate Cancer  
769 Research, the Prostate Cancer Foundation, NCI SPORE 1P50CA275741, and Department of Defense  
770 awards W81XWH-22-1-0833 and HT94252410252. This work was supported by the Office of the  
771 Assistant Secretary of Defense for Health Affairs through the Prostate Cancer Research Program under  
772 Award No. HT94252410123.

773

774 **Author Contributions**

775 P.T. and M.A.R. conceived the project and designed all studies in the project. P.T., with assistance of  
776 I.P., P.D.R., A.N., and L.M., performed most wet-lab experiments. M.S. performed ATAC-seq, B.D.

777 performed ChIP-seq. A.B., X.Y., and Ju.T. are professional bioinformaticians and conducted data  
778 acquisition, analysis, and interpretation of RNA-seq, scRNA-seq, ATAC-seq, ChIP-seq, and PRO-cap.  
779 S.R.S. performed PRO-cap library preparation. A.K.L assisted with PRO-cap bioinformatic analysis. N.L.,  
780 D.A.Q. and I.P. performed Hi-C enhancer-promoter analysis. M.L. performed animal experiments. S.d.B  
781 conducted histopathological evaluation. Jo.T. performed histopathological data analysis. G.C. and M.B.  
782 performed bioinformatic CRPC signature score evaluation in scRNA-seq data curated from commercially  
783 available data. H.B. and Y.C. provided PCa organoid models. S.P. and C.N. provided expert commentary  
784 and bioinformatic expertise. H.Y. provided expert commentary and supervision of PRO-Cap experiment.  
785 R.L.Y. provided resources, relevant data, and expert commentary. P.T. and M.A.R. wrote the manuscript  
786 with the help of Jo.T.

787 **References**

788 1. Bluemn, E.G. *et al.* Androgen Receptor Pathway-Independent Prostate Cancer Is Sustained  
789 through FGF Signaling. *Cancer Cell* **32**, 474-489 e6 (2017).

790 2. Chan, J.M. *et al.* Lineage plasticity in prostate cancer depends on JAK/STAT inflammatory  
791 signaling. *Science* **377**, 1180-1191 (2022).

792 3. Beltran, H. *et al.* Divergent clonal evolution of castration-resistant neuroendocrine prostate  
793 cancer. *Nat Med* **22**, 298-305 (2016).

794 4. Ye, Y., Chen, X. & Zhang, W. Mammalian SWI/SNF Chromatin Remodeling Complexes in  
795 Embryonic Stem Cells: Regulating the Balance Between Pluripotency and Differentiation. *Front  
796 Cell Dev Biol* **8**, 626383 (2020).

797 5. Hodges, C., Kirkland, J.G. & Crabtree, G.R. The Many Roles of BAF (mSWI/SNF) and PBAF  
798 Complexes in Cancer. *Cold Spring Harb Perspect Med* **6**(2016).

799 6. Cyrtà, J. *et al.* Role of specialized composition of SWI/SNF complexes in prostate cancer lineage  
800 plasticity. *Nature Communications* **11**, 5549 (2020).

801 7. Rubin, M.A., Bristow, R.G., Thienger, P.D., Dive, C. & Imielinski, M. Impact of Lineage Plasticity  
802 to and from a Neuroendocrine Phenotype on Progression and Response in Prostate and Lung  
803 Cancers. *Molecular Cell* **80**, 562-577 (2020).

804 8. Xue, Y. *et al.* SMARCA4 loss is synthetic lethal with CDK4/6 inhibition in non-small cell lung  
805 cancer. *Nat Commun* **10**, 557 (2019).

806 9. Cantley, J. *et al.* Selective PROTAC-mediated degradation of SMARCA2 is efficacious in  
807 SMARCA4 mutant cancers. *Nat Commun* **13**, 6814 (2022).

808 10. Hoffman, G.R. *et al.* Functional epigenetics approach identifies BRM/SMARCA2 as a critical  
809 synthetic lethal target in BRG1-deficient cancers. *Proc Natl Acad Sci U S A* **111**, 3128-33 (2014).

810 11. Xiao, L. *et al.* Targeting SWI/SNF ATPases in enhancer-addicted prostate cancer. *Nature* **601**,  
811 434-439 (2022).

812 12. Griffin, C.T., Curtis, C.D., Davis, R.B., Muthukumar, V. & Magnuson, T. The chromatin-remodeling  
813 enzyme BRG1 modulates vascular Wnt signaling at two levels. *Proc Natl Acad Sci U S A* **108**,  
814 2282-7 (2011).

815 13. Park, J.I. *et al.* Telomerase modulates Wnt signalling by association with target gene chromatin.  
816 *Nature* **460**, 66-72 (2009).

817 14. Wang, Y. *et al.* The long noncoding RNA IncTCF7 promotes self-renewal of human liver cancer  
818 stem cells through activation of Wnt signaling. *Cell Stem Cell* **16**, 413-25 (2015).

819 15. Murillo-Garzon, V. & Kypta, R. WNT signalling in prostate cancer. *Nat Rev Urol* **14**, 683-696  
820 (2017).

821 16. Miyamoto, D.T. *et al.* RNA-Seq of single prostate CTCs implicates noncanonical Wnt signaling in  
822 antiandrogen resistance. *Science* **349**, 1351-6 (2015).

823 17. Korinek, V. *et al.* Constitutive transcriptional activation by a beta-catenin-Tcf complex in APC-/-  
824 colon carcinoma. *Science* **275**, 1784-7 (1997).

825 18. Zhan, T., Rindtorff, N. & Boutros, M. Wnt signaling in cancer. *Oncogene* **36**, 1461-1473 (2017).

826 19. Sandmark, E. *et al.* A novel non-canonical Wnt signature for prostate cancer aggressiveness.  
827 *Oncotarget* **8**, 9572-9586 (2017).

828 20. Grasso, C.S. *et al.* The mutational landscape of lethal castration-resistant prostate cancer. *Nature*  
829 **487**, 239-43 (2012).

830 21. Zong, Y. *et al.* Stromal epigenetic dysregulation is sufficient to initiate mouse prostate cancer via  
831 paracrine Wnt signaling. *Proc Natl Acad Sci U S A* **109**, E3395-404 (2012).

832 22. Li, X. *et al.* Prostate tumor progression is mediated by a paracrine TGF-beta/Wnt3a signaling axis.  
833 *Oncogene* **27**, 7118-30 (2008).

834 23. Tang, F. *et al.* Chromatin profiles classify castration-resistant prostate cancers suggesting  
835 therapeutic targets. *Science* **376**, eabe1505 (2022).

836 24. Ding, Y. *et al.* Chromatin remodeling ATPase BRG1 and PTEN are synthetic lethal in prostate  
837 cancer. *The Journal of Clinical Investigation* **129**, 759-773 (2019).

838 25. Dong, B. *et al.* Single-cell analysis supports a luminal-neuroendocrine transdifferentiation in  
839 human prostate cancer. *Commun Biol* **3**, 778 (2020).

840 26. Kfouri, Y. *et al.* Human prostate cancer bone metastases have an actionable immunosuppressive  
841 microenvironment. *Cancer Cell* **39**, 1464-1478 e8 (2021).

842 27. Heidegger, I. *et al.* Comprehensive characterization of the prostate tumor microenvironment  
843 identifies CXCR4/CXCL12 crosstalk as a novel antiangiogenic therapeutic target in prostate  
844 cancer. *Mol Cancer* **21**, 132 (2022).

845 28. Hirz, T. *et al.* Dissecting the immune suppressive human prostate tumor microenvironment via  
846 integrated single-cell and spatial transcriptomic analyses. *Nat Commun* **14**, 663 (2023).

847 29. Ma, X. *et al.* Identification of a distinct luminal subgroup diagnosing and stratifying early stage  
848 prostate cancer by tissue-based single-cell RNA sequencing. *Mol Cancer* **19**, 147 (2020).

849 30. Muraro, M.J. *et al.* A Single-Cell Transcriptome Atlas of the Human Pancreas. *Cell Syst* **3**, 385-  
850 394 e3 (2016).

851 31. Aibar, S. *et al.* SCENIC: single-cell regulatory network inference and clustering. *Nat Methods* **14**,  
852 1083-1086 (2017).

853 32. Gan, X.Q. *et al.* Nuclear Dvl, c-Jun, beta-catenin, and TCF form a complex leading to stabilization  
854 of beta-catenin-TCF interaction. *J Cell Biol* **180**, 1087-100 (2008).

855 33. Toualbi, K. *et al.* Physical and functional cooperation between AP-1 and beta-catenin for the  
856 regulation of TCF-dependent genes. *Oncogene* **26**, 3492-502 (2007).

857 34. Nateri, A.S., Spencer-Dene, B. & Behrens, A. Interaction of phosphorylated c-Jun with TCF4  
858 regulates intestinal cancer development. *Nature* **437**, 281-5 (2005).

859 35. Guo, Q. *et al.* A beta-catenin-driven switch in TCF/LEF transcription factor binding to DNA target  
860 sites promotes commitment of mammalian nephron progenitor cells. *Elife* **10**(2021).

861 36. Park, J.S. *et al.* Six2 and Wnt regulate self-renewal and commitment of nephron progenitors  
862 through shared gene regulatory networks. *Dev Cell* **23**, 637-51 (2012).

863 37. Leppanen, N. *et al.* SIX2 promotes cell plasticity via Wnt/beta-catenin signalling in androgen  
864 receptor independent prostate cancer. *Nucleic Acids Res* **52**, 5610-5623 (2024).

865 38. Tierney, M.T. *et al.* Vitamin A resolves lineage plasticity to orchestrate stem cell lineage choices.  
866 *Science* **383**, eadi7342 (2024).

867 39. Schick, S. *et al.* Acute BAF perturbation causes immediate changes in chromatin accessibility.  
868 *Nat Genet* **53**, 269-278 (2021).

869 40. Iurlaro, M. *et al.* Mammalian SWI/SNF continuously restores local accessibility to chromatin. *Nat*  
870 *Genet* **53**, 279-287 (2021).

871 41. Yao, L. *et al.* A comparison of experimental assays and analytical methods for genome-wide  
872 identification of active enhancers. *Nat Biotechnol* **40**, 1056-1065 (2022).

873 42. Tippens, N.D. *et al.* Transcription imparts architecture, function and logic to enhancer units. *Nat*  
874 *Genet* **52**, 1067-1075 (2020).

875 43. Layer, R.M. *et al.* GIGGLE: a search engine for large-scale integrated genome analysis. *Nat*  
876 *Methods* **15**, 123-126 (2018).

877 44. Zhao, S.G. *et al.* Integrated analyses highlight interactions between the three-dimensional  
878 genome and DNA, RNA and epigenomic alterations in metastatic prostate cancer. *Nat Genet* **56**,  
879 1689-1700 (2024).

880 45. Savic, D. *et al.* Alterations in TCF7L2 expression define its role as a key regulator of glucose  
881 metabolism. *Genome Res* **21**, 1417-25 (2011).

882 46. Savic, D., Park, S.Y., Bailey, K.A., Bell, G.I. & Nobrega, M.A. In vitro scan for enhancers at the  
883 TCF7L2 locus. *Diabetologia* **56**, 121-5 (2013).

884 47. Veeman, M.T., Slusarski, D.C., Kaykas, A., Louie, S.H. & Moon, R.T. Zebrafish prickle, a  
885 modulator of noncanonical Wnt/Fz signaling, regulates gastrulation movements. *Curr Biol* **13**,  
886 680-5 (2003).

887 48. Liu, J. *et al.* Targeting Wnt-driven cancer through the inhibition of Porcupine by LGK974. *Proc*  
888 *Natl Acad Sci U S A* **110**, 20224-9 (2013).

889 49. Gonsalves, F.C. *et al.* An RNAi-based chemical genetic screen identifies three small-molecule  
890 inhibitors of the Wnt/wingless signaling pathway. *Proc Natl Acad Sci U S A* **108**, 5954-63 (2011).

891 50. Hwang, S.Y. *et al.* Direct Targeting of beta-Catenin by a Small Molecule Stimulates Proteasomal  
892 Degradation and Suppresses Oncogenic Wnt/beta-Catenin Signaling. *Cell Rep* **16**, 28-36 (2016).

893 51. Wagle, M.C. *et al.* A transcriptional MAPK Pathway Activity Score (MPAS) is a clinically relevant  
894 biomarker in multiple cancer types. *NPJ Precis Oncol* **2**, 7 (2018).

895 52. Shtutman, M. *et al.* The cyclin D1 gene is a target of the beta-catenin/LEF-1 pathway. *Proc Natl  
896 Acad Sci U S A* **96**, 5522-7 (1999).

897 53. Labbe, D.P. & Brown, M. Transcriptional Regulation in Prostate Cancer. *Cold Spring Harb  
898 Perspect Med* **8**(2018).

899 54. Yamada, Y. & Beltran, H. Clinical and Biological Features of Neuroendocrine Prostate Cancer.  
900 *Curr Oncol Rep* **23**, 15 (2021).

901 55. Neiheisel, A., Kaur, M., Ma, N., Havard, P. & Shenoy, A.K. Wnt pathway modulators in cancer  
902 therapeutics: An update on completed and ongoing clinical trials. *Int J Cancer* **150**, 727-740  
903 (2022).

904 56. Luo, M. *et al.* Advances of targeting the YAP/TAZ-TEAD complex in the hippo pathway for the  
905 treatment of cancers. *Eur J Med Chem* **244**, 114847 (2022).

906 57. Centore, R.C. *et al.* Pharmacologic inhibition of BAF chromatin remodeling complexes as a  
907 therapeutic approach to transcription factor-dependent cancers. *bioRxiv*, 2023.09.11.557162  
908 (2023).

909 58. Kundu, S. *et al.* Linking FOXO3, NCOA3, and TCF7L2 to Ras pathway phenotypes through a  
910 genome-wide forward genetic screen in human colorectal cancer cells. *Genome Med* **10**, 2  
911 (2018).

912 59. Nickols, N.G. *et al.* MEK-ERK signaling is a therapeutic target in metastatic castration resistant  
913 prostate cancer. *Prostate Cancer Prostatic Dis* **22**, 531-538 (2019).

914 60. He, T. *et al.* Targeting the mSWI/SNF Complex in POU2F-POU2AF Transcription Factor-Driven  
915 Malignancies. *bioRxiv* (2024).

916 61. Gao, D. *et al.* Organoid cultures derived from patients with advanced prostate cancer. *Cell* **159**,  
917 176-187 (2014).

918 62. Mu, P. *et al.* SOX2 promotes lineage plasticity and antiandrogen resistance in TP53- and RB1-  
919 deficient prostate cancer. *Science* **355**, 84-88 (2017).

920 63. Kaminow, B., Yunusov, D. & Dobin, A. STARsolo: accurate, fast and versatile  
921 mapping/quantification of single-cell and single-nucleus RNA-seq data. *bioRxiv*,  
922 2021.05.05.442755 (2021).

923 64. Stuart, T. *et al.* Comprehensive Integration of Single-Cell Data. *Cell* **177**, 1888-1902 e21 (2019).

924 65. Butler, A., Hoffman, P., Smibert, P., Papalexi, E. & Satija, R. Integrating single-cell transcriptomic  
925 data across different conditions, technologies, and species. *Nat Biotechnol* **36**, 411-420 (2018).

926 66. Satija, R., Farrell, J.A., Gennert, D., Schier, A.F. & Regev, A. Spatial reconstruction of single-cell  
927 gene expression data. *Nat Biotechnol* **33**, 495-502 (2015).

928 67. McCarthy, D.J., Campbell, K.R., Lun, A.T. & Wills, Q.F. Scater: pre-processing, quality control,  
929 normalization and visualization of single-cell RNA-seq data in R. *Bioinformatics* **33**, 1179-1186  
930 (2017).

931 68. McGinnis, C.S., Murrow, L.M. & Gartner, Z.J. DoubletFinder: Doublet Detection in Single-Cell  
932 RNA Sequencing Data Using Artificial Nearest Neighbors. *Cell Syst* **8**, 329-337 e4 (2019).

933 69. Zappia, L. & Oshlack, A. Clustering trees: a visualization for evaluating clusterings at multiple  
934 resolutions. *Gigascience* **7**(2018).

935 70. Finak, G. *et al.* MAST: a flexible statistical framework for assessing transcriptional changes and  
936 characterizing heterogeneity in single-cell RNA sequencing data. *Genome Biol* **16**, 278 (2015).

937 71. Wolf, F.A., Angerer, P. & Theis, F.J. SCANPY: large-scale single-cell gene expression data  
938 analysis. *Genome Biol* **19**, 15 (2018).

939 72. Hao, Y. *et al.* Integrated analysis of multimodal single-cell data. *Cell* **184**, 3573-3587 e29 (2021).

940 73. Korotkevich, G. *et al.* Fast gene set enrichment analysis. *bioRxiv*, 060012 (2021).

941 74. Van de Sande, B. *et al.* A scalable SCENIC workflow for single-cell gene regulatory network  
942 analysis. *Nat Protoc* **15**, 2247-2276 (2020).

943 75. Dobin, A. *et al.* STAR: ultrafast universal RNA-seq aligner. *Bioinformatics* **29**, 15-21 (2012).

944 76. Li, B. & Dewey, C.N. RSEM: accurate transcript quantification from RNA-Seq data with or without  
945 a reference genome. *BMC Bioinformatics* **12**, 323 (2011).

946 77. Love, M.I., Huber, W. & Anders, S. Moderated estimation of fold change and dispersion for RNA-  
947 seq data with DESeq2. *Genome Biol* **15**, 550 (2014).

948 78. Hagenbeek, T.J. *et al.* An allosteric pan-TEAD inhibitor blocks oncogenic YAP/TAZ signaling and  
949 overcomes KRAS G12C inhibitor resistance. *Nat Cancer* **4**, 812-828 (2023).

950 79. Kwak, H., Fuda, N.J., Core, L.J. & Lis, J.T. Precise maps of RNA polymerase reveal how  
951 promoters direct initiation and pausing. *Science* **339**, 950-3 (2013).

952 80. Mahat, D.B. *et al.* Base-pair-resolution genome-wide mapping of active RNA polymerases using  
953 precision nuclear run-on (PRO-seq). *Nature Protocols* **11**, 1455-1476 (2016).

954 81. Cotter, K.A. *et al.* Capped nascent RNA sequencing reveals novel therapy-responsive enhancers  
955 in prostate cancer. *bioRxiv*, 2022.04.08.487666 (2022).

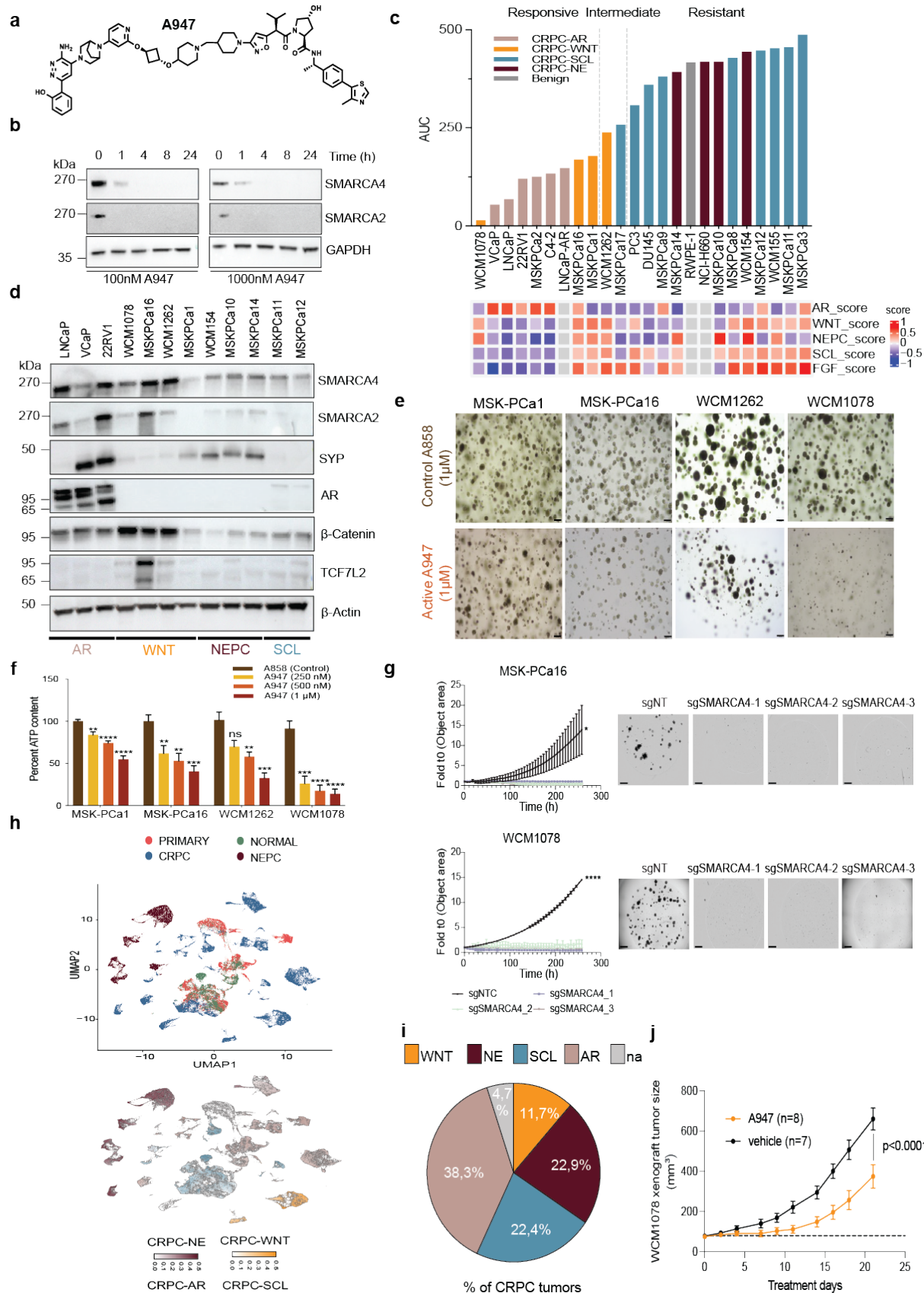
956

957

958 **Table1.** Publicly available datasets were analyzed in this study.

Dataset ID	Number of samples	Sample type	Sequencing platform and chemistry	Reference (DOI)
GSE137829	6	CRPC	10x Genomics 3' v2	10.1038/s42003-020-01476-1 <sup>25</sup>
GSE143791	9	CRPC	10x Genomics 3' v2	10.1016/j.ccell.2021.09.005 <sup>26</sup>
GSE157703	2	Primary tumor	10x Genomics 3' v3	10.1186/s12943-020-01264-9 <sup>29</sup>
GSE181294	35	Primary tumor and normal adjacent tissue	10x Genomics 3' v2	10.1038/s41467-023-36325-2 <sup>28</sup>
GSE193337	8	Primary tumor and normal adjacent tissue	10x Genomics 3' v3	10.1186/s12943-022-01597-7 <sup>27</sup>
GSE210358	14	CRPC	10x Genomics 3' v3	10.1126/science.abn0478 <sup>2</sup>

959



961 a, Structure of A947 SMARCA2/4 PROTAC degrader.

962 b, Immunoblot of indicated proteins in HEK293 cells treated with A947 (0.1 $\mu$ M or 1 $\mu$ M) or DMSO over  
963 indicated time course. GAPDH represents loading control and is probed in a representative immunoblot  
964 (n=2 independent immunoblots).

965 c, Area under the curve (AUC) of A947 dose response curves (see Supp. figure 1a and b) in a panel of  
966 human-derived prostate cancer or normal cell lines after 7 days of treatment. Viability was assessed  
967 using Celltiter Glo 2.0. Heatmap indicates gene-set scores per cell model using Tang et al.<sup>23</sup> scores. Data  
968 is representative of at least n = 3 independent experiments.

969 d, Immunoblot of indicated proteins in a panel of PCa organoids representing different phenotypes.  $\beta$ -  
970 Actin serves as a loading control and is probed in a representative immunoblot (n=1).

971 e, Brightfield microscopy of indicated PCa organoids after 10 days of treatment with A947 (1 $\mu$ M) or  
972 epimer control A858 (1 $\mu$ M). Scale bars: 20  $\mu$ m.

973 f, Proliferation of indicated PCa organoids after 10 days of treatment with A947 (at 0.25 $\mu$ M, 0.5 $\mu$ M, 1 $\mu$ M)  
974 or epimer control A858 (1 $\mu$ M) measured by Celltiter Glo 3D (n = 3 independent biological experiments).  
975 Data are presented as mean values +/- SEM and analyzed using unpaired Students t-test (\*p < 0.05,  
976 \*\*p < 0.01, \*\*\*p < 0.001, \*\*\*\*p < 0.0001). Data is representative of at least n = 3 independent  
977 experiments.

978 g, Spheroid formation of indicated PCa organoids transduced with CRISPRi-Cas9 guide RNA (sgRNA)  
979 against SMARCA4 measured by live imaging using Incucyte SX5. N = 3 independent experiments.  
980 Brightfield microscopy of indicated PCa organoids at Incucyte assay endpoint, Scale bars: 800  $\mu$ m. Data  
981 are presented as mean values +/- SEM and analyzed using two-way ANOVA (\*p < 0.05, \*\*p < 0.01,  
982 \*\*\*p < 0.001, \*\*\*\*p < 0.0001). Data is representative of n = 2 independent experiments.

983 h, UMAP plot showing disease classification (left) and relative expression of indicated signature gene  
984 scores (right) in 74 samples from six distinct PCa scRNAseq studies<sup>2,25-29</sup>. Side annotations indicate the  
985 AR score, NE score, stem cell-like (SCL) score, and WNT score, as determined by Tang et al.<sup>23</sup>,

986 compared with pathology classification and molecular subtypes of each sample. False discovery rate  
987 (FDR) <0.05.

988 i, Percentage of indicated signatures found among all CRPC classified samples displayed as a pie chart.

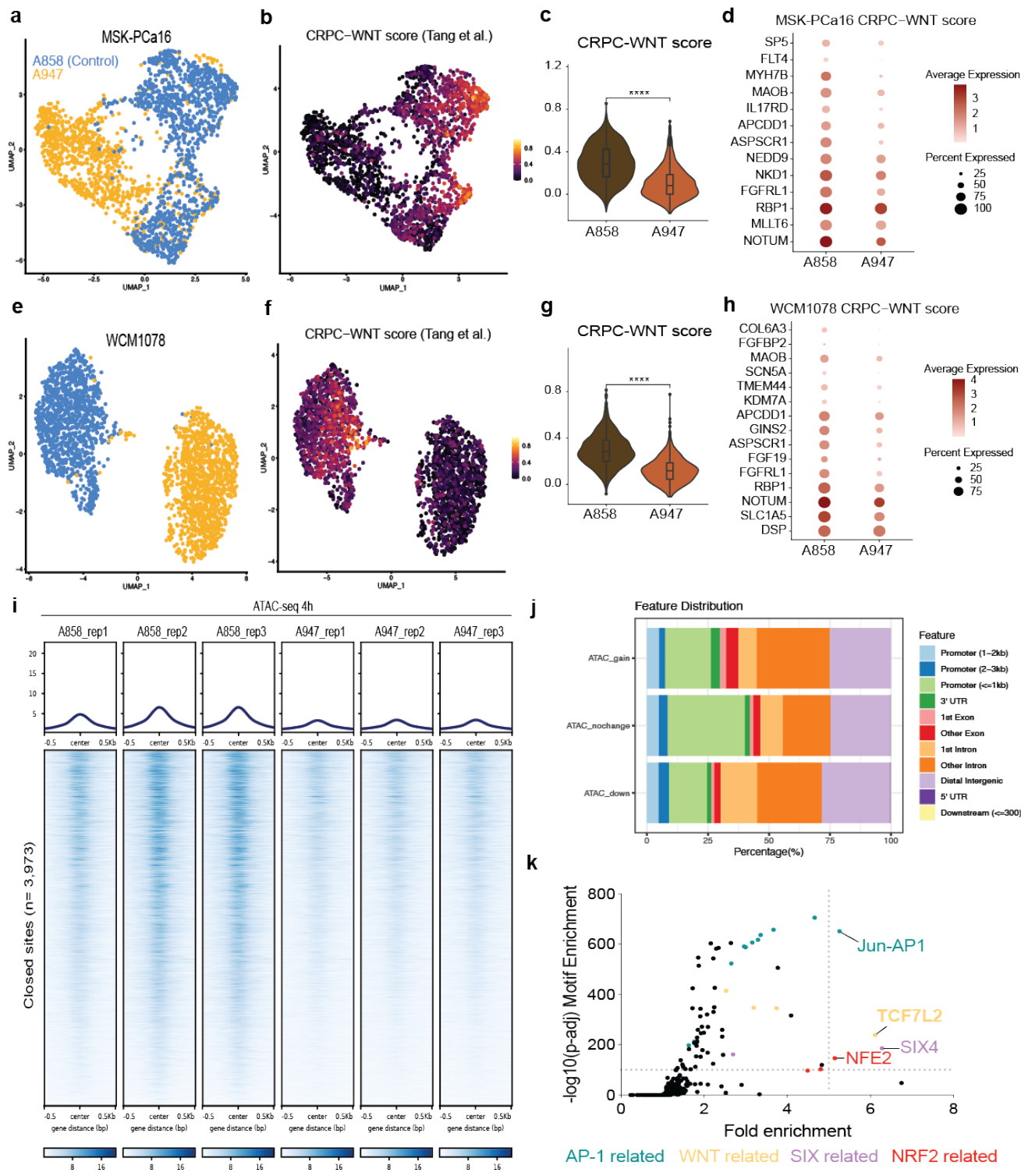
989 Not announced (na).

990 j, Tumor growth of WCM1078 PDX subline treated with vehicle (n=7) or 40mg/kg A947 (n=8) in xx mice.

991 Data are presented as mean values +/- SEM and analyzed using two-way ANOVA (p < 0.0001).

992

993



994 **Fig. 2 SMARCA2/4 degradation leads to strong downregulation and chromatin compaction of**  
995 **CRPC-WNT lineage-characterizing genes**

996 a, UMAP plot of MSK-PCa16 organoids treated with either 1 $\mu$ M A858 (blue) or 1 $\mu$ M A947 (yellow) for  
997 72h.

998 b, UMAP plot of MSK-PCa16 organoids treated with either 1 $\mu$ M A858 or 1 $\mu$ M A947 for 72h displaying  
999 CRPC-WNT signature score<sup>23</sup>.

1000 c, Violin plot of MSK-PCa16 organoids treated with 1 $\mu$ M A858 or 1 $\mu$ M A947 for 72h displaying CRPC-  
1001 WNT signature<sup>23</sup> signature score. Analyzed using the Wilcoxon test (\*\*\*\*p < 0.0001).

1002 d, Bubble plot indicative of expression levels of top 10 deregulated CRPC-WNT signature genes<sup>23</sup> in  
1003 MSK-PCa16 organoids treated with 1 $\mu$ M A858 or 1 $\mu$ M A947 for 72h.

1004 e, UMAP plot of WCM1078 organoids treated with 1 $\mu$ M A858 (blue) or 1 $\mu$ M A947 (yellow) for 72h.

1005 f, UMAP plot of WCM1078 organoids treated with 1 $\mu$ M A858 or 1 $\mu$ M A947 for 72h displaying CRPC-WNT  
1006 signature score<sup>23</sup>.

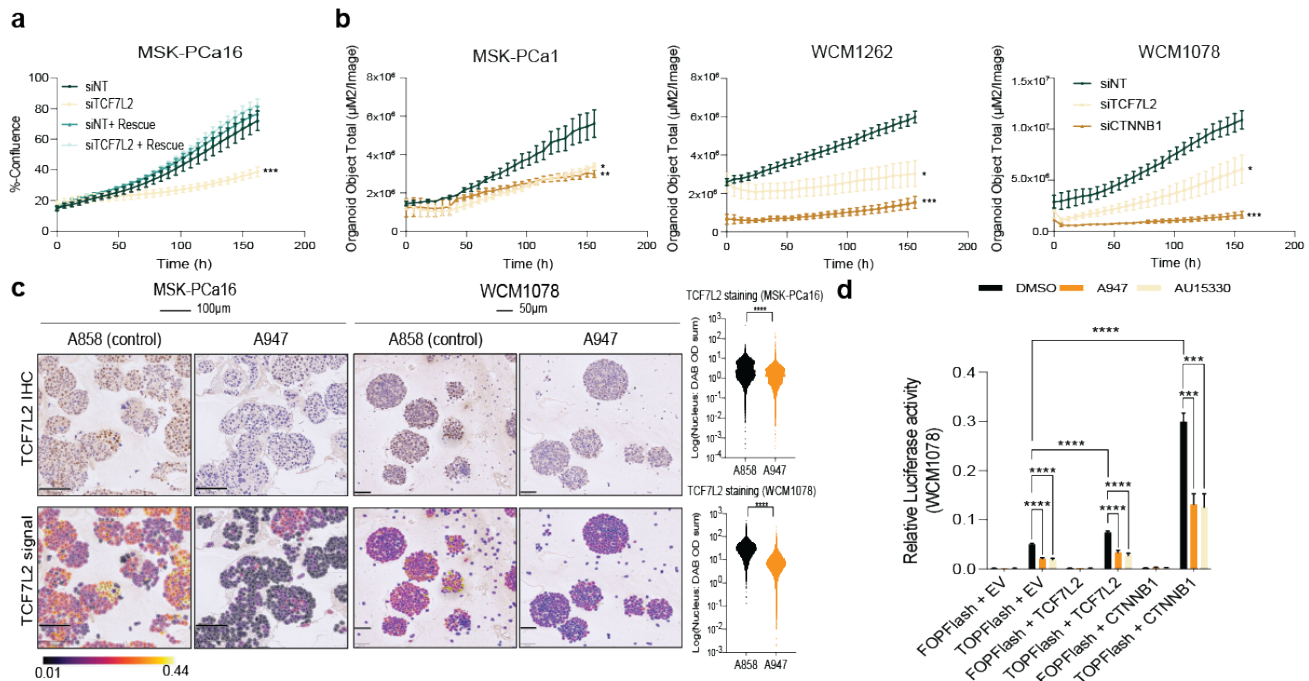
1007 g, Violin plot of WCM1078 organoids treated with 1 $\mu$ M A858 or 1 $\mu$ M A947 for 72h displaying CRPC-WNT  
1008 signature<sup>23</sup> signature score. Analyzed using the Wilcoxon test (\*\*\*\*p < 0.0001).

1009 h, Bubble plot indicative of expression levels of top 10 deregulated CRPC-WNT signature genes<sup>23</sup> in  
1010 WCM1078 organoids treated with 1 $\mu$ M A858 or 1 $\mu$ M A947 for 72h.

1011 i, ATAC-seq read-density tornado plots from WCM1078 organoids treated with 1 $\mu$ M A858 or 1 $\mu$ M A947  
1012 for 4h (n = 3 biological replicates). Venn diagram indicating lost regions.

1013 j, Genome-wide changes in chromatin accessibility upon A947-treatment for 4 h in WCM1078 organoids  
1014 along with genomic annotation of sites that gain (gained) or lose accessibility (lost) or remain unaltered  
1015 (unchanged).

1016 k, Motifs enriched in depleted peaks from WCM1078 treated for 4h with 1 $\mu$ M A947 identified using  
1017 HOMER on ATAC-seq.



1018

### Fig.3 TCF7L2 is a dependency in CRPC-WNT

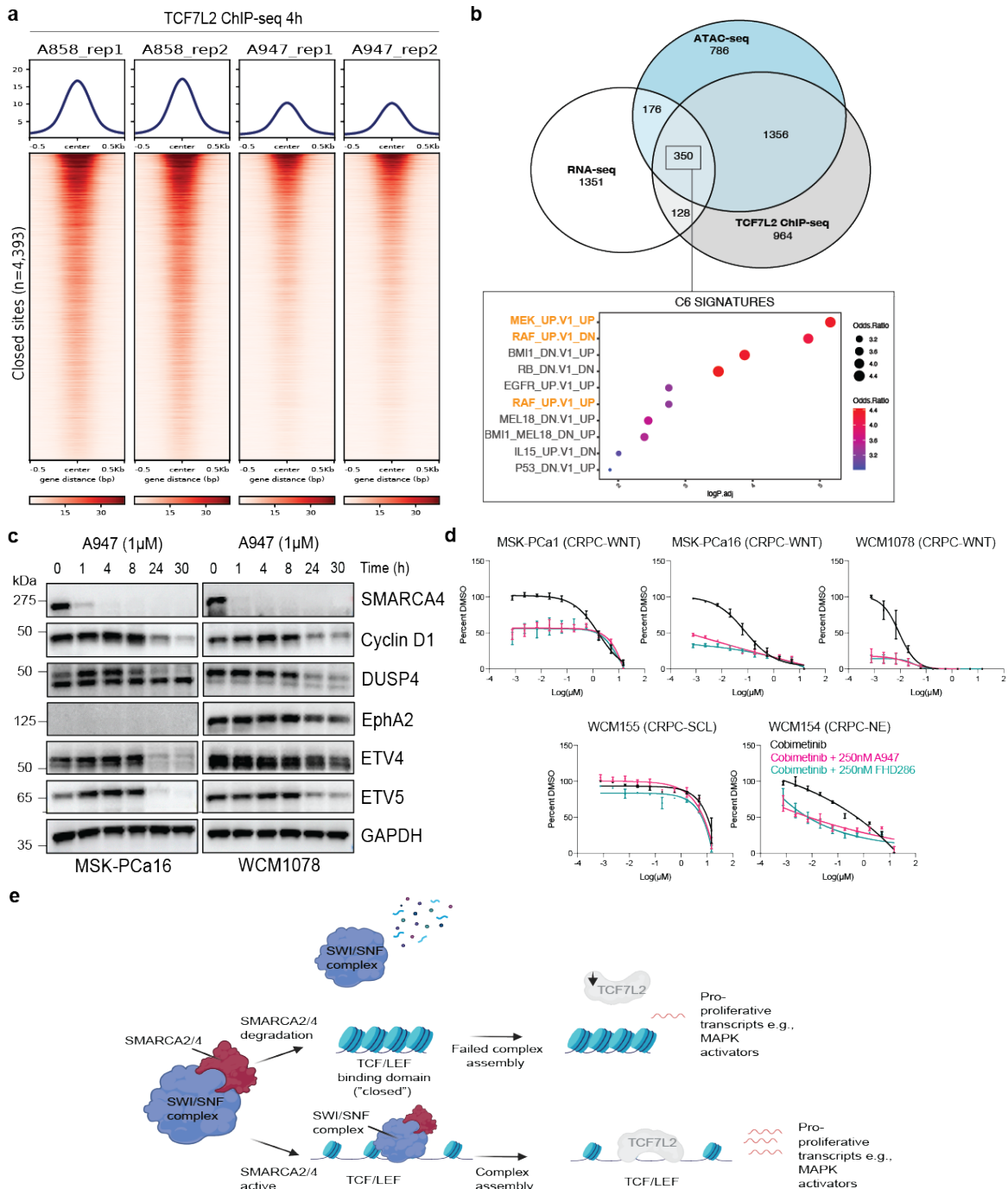
1019 a, Growth data measured by live-cell imaging (Incucyte S3) upon transfection of indicated siRNA or  
1020 plasmid (EV or rescue). Immunoblot of indicated proteins at 72h after transfection. GAPDH serves as  
1021 loading control. Data are presented as mean values +/- SEM and analyzed using two-way ANOVA  
1022 (\*p < 0.05, \*\*p < 0.01, \*\*\*p < 0.001). Data is representative of n = 2 independent experiments. EV: empty  
1023 vector.

1024 b, Spheroid formation measured by live-cell imaging (Incucyte SX5) upon transfection of indicated siRNA.  
1025 Data are presented as mean values +/- SEM and analyzed using two-way Anova (\*p < 0.05, \*\*p < 0.01,  
1026 \*\*\*p < 0.001). Data is representative of n = 2 independent experiments. EV: empty vector.

1027 c, Immunohistochemistry (IHC) and staining intensity of TCF7L2 on indicated organoids upon treatment  
1028 with 1 $\mu\text{M}$  A858 or 1 $\mu\text{M}$  A947 for 24h. Violin plot from TCF7L2 staining intensity analyzed using two-way  
1029 ANOVA (\*p < 0.05, \*\*p < 0.01, \*\*\*p < 0.001, \*\*\*\*p < 0.0001). Scale: 100 $\mu\text{m}$  (MSK-PCa16), 50 $\mu\text{m}$   
1030 (WCM1078).

1031 d, TOPFlash TCF/LEF reporter assay measured after 48h upon treatment with indicated drugs in  
1032 WCM1078 sublines. FOPFlash serves as a negative reporter control. Data are presented as mean

1033 values +/- SEM after normalization to internal Renilla control and analyzed using paired Students t-test  
1034 (\*\*p < 0.001, \*\*\*\*p < 0.0001). Data is representative of  $n = 2$  independent experiments. EV: empty vector,  
1035 OE: overexpression.



1036 **Fig.4 TCF7L2 regulates a pro-proliferative signatures in CRPC-WNT**

1037 a, ChIP-seq read-density tornado plots from WCM1078 organoids treated with 1 $\mu$ M A858 or 1 $\mu$ M A947  
 1038 for 4h ( $n = 2$  biological replicates). Venn diagram indicating lost regions.

1039 b, Venn diagram indicating A947-treated lost regions from ChIP-seq, ATAC-seq and RNA-seq data in  
1040 WCM1078. GSEA analysis was performed from 350 overlapping genes.

1041 c, Immunoblot of indicated proteins at indicated time upon treatment with 1 $\mu$ M A947. GAPDH serves as  
1042 loading control. Data is representative of  $n = 2$  independent experiments.

1043 d, Dose-response curves with indicated drugs after measurement of proliferation with Celltiter Glo 2.0  
1044 after 7-day treatment ( $n=2$  independent experiments).

1045 e, Model of mechanism. SMARCA4-containing SWI/SNF complex maintains open chromatin  
1046 confirmation of TCF binding domains in CRPC-WNT. TCF7L2 positively regulates lineage-specific  
1047 programs that orchestrate CRPC-WNT proliferation and survival. TFC7L2 cannot bind to the chromatin  
1048 when SWISNF ATPase activity is impaired. In addition, loss of SWI/SNF ATPases leads to  
1049 downregulation of TCF7L2 transcript protein levels. Figure created with Biorender.com.

1050